A REVIEW OF THE INTEGRITY OF METALLIC VEHICLE ARMOUR TO PROJECTILE ATTACK

D. Lenihan[1], W. Ronan[2], P.E. O'Donoghue[3], S.B. Leen[1]

[1]*Mechanical Engineering, NUI Galway*

[2]*Biomedical Engineering, NUI Galway*

[3]*Civil Engineering, NUI Galway*

Corresponding Author: Donncha Lenihan. *donncha.lenihan@gmail.com*

Abstract: This article presents a review of engineering and design aspects relevant to the mechanical and structural integrity of military vehicular armour, including materials-related technologies. Theoretical, experimental and numerical techniques for assessment are discussed and evaluated. A number of prominent material constitutive models are comparatively assessed. The Johnson-Cook model is shown to be particularly consistent in terms of agreement with experimental data, identification of material constants and ease of application. The article also discusses different numerical codes used and their relevance over time. Finally, it is argued that there is a need for a materials design tool for military vehicular armour.

Keywords: armour, projectile, terminal ballistics, impact, protection, military vehicles

1. Introduction

An Armoured Fighting Vehicle (AFV) is a military vehicle with a hull specifically designed to resist penetration from enemy weapons, thus allowing it to move more freely in the battlespace. AFVs are used for a wide variety of roles, from full-scale assault on enemy positions to quickly laying down temporary bridges so that friendly vehicles can cross a river. Since World War I,

when AFVs were first developed and used [1], the development of their armour has gone hand-in-hand with the development of anti-armour weapons. The crew and other personnel in an AFV, while protected from the majority of battlefield threats, are nevertheless in danger due to being more conspicuous, less mobile and representing a high-value target for the enemy. Attacks on vehicle-mounted troops have a different profile of wounding and lethality than attacks on dismounted troops [2], and in recent conflicts have accounted for the majority of casualties [3]. Vehicular armour is required to provide a high level of protection but with minimum effect on vehicle size and weight. It is incumbent, therefore, on the designer of armour to ensure that the response of the armour material to various battlefield threats can be quantified and evaluated effectively.

This paper provides an overview of the engineering aspects of armour design, by focusing on the most common threats to AFVs and the mechanisms of failure. The study of high-speed projectile impact on armour, known as terminal ballistics, deals primarily with impacts which occur in the 'ordnance range', i.e. roughly 500 to 2000 m/s. In addition to this, much interest is also focused on the behaviour of shaped charge jets, which impact with velocities between 2000 and 8000 m/s [4]. This is obviously a very broad spectrum and there is a wealth of more specific analyses of each of the velocity regions mentioned.

This review is organised as follows: (i) The classes of materials, mostly metals, in use for armour and projectile applications are introduced. (ii) The three main types of armour defeat mechanisms are described: rigid penetration, hydrodynamic penetration and spalling. There are other ways in which armour is defeated, e.g. blast waves. However, these are considered to be outside the scope of this review. (iii) Some key experimental techniques used for terminal ballistics are considered, focusing in detail on the effects of spalling. (iv) Material models used for analytical and numerical quantification of the deformation, damage and subsequent failure of armour materials during impact events are reviewed. (v) The numerical aspects of terminal

ballistics and various techniques and specific analysis codes used to simulate impact events are reviewed. The increasing possibility in more recent years to model at smaller scales will also be discussed. This allows the capture of the microstructural behaviour of materials, thus providing additional insights on the armour failure process. (vi) Finally, future trends in armour design and analysis are discussed.

2. Armour materials

There is no worldwide standard for general armour steels or materials [5]. Much of the technical information associated with military armour is proprietary or classified for security reasons. There are, however, standard levels of armour protection. NATO, for example, have developed a STANAG (STANdard AGreement) document describing these levels [6], which was recently updated to take account of the increasing lethality of some forms of kinetic energy ammunition [7]. It is important to note that metallic materials (including those used as armour) behave differently under dynamic loading conditions than under static conditions. For example, the flow stress is more sensitive to the strain rate observed, and thermal softening weakens the material due to adiabatic heating [8]. As a result, the optimal metal austenising and tempering temperatures for ballistic performance differ from those for static strength and hardness [5]. The primary function of armour material is to resist the various mechanisms of defeat, which will be discussed further in Section 3.

A distinction can be made between 'energy disruptive' and 'energy absorbing' armour materials [9]. The 'disruptive' material is intended to induce fragmentation in the penetrator, thus dispersing its kinetic energy, while the 'absorber' transfers the kinetic energy of the projectile to heat [10]. In general, ceramics and metals with a high hardness are disruptive and metals with large ductility and toughness are absorbing.

Traditionally, and continually, armoured vehicles have been fabricated from high-strength steels, generally with 0.25 to 0.4 per cent carbon. The principal alloying elements are chromium (which increases hardness) and nickel (which increases toughness) [11]. The tensile strength of such steels has varied from 850 to 1700 MPa. Although it can be cast into complete shapes, such as vehicle turrets, amour is usually produced in the form of Rolled Homogeneous Armour (RHA) [12]. The tempering process used after the heat treatment gives the armour a uniform microstructure, hence the 'homogeneous' designation [9]. An alternative to RHA is homogeneous high-hardness armour (HHA), which uses low-alloy steels, heat-treated to give increased hardness. The tempering temperatures for this material are lower than for RHA [9]. Although the resulting material is very brittle, which initially caused problems even without projectile impacts, this problem has been overcome through improved processing techniques and material composition [12]. A technique which combines the advantageous ductility and toughness of RHA (i.e. an 'absorber' material) with the 'disruptive' qualities of high-hardness armour is dual hardness armour, which is created by roll-bonding two separate plates together into a single plate of armour (for example, a plate of HHA bonded to the front of a plate of RHA). This technique can produce armour which is 78% more effective (using a metric such as the material mass efficiency [5]) per unit weight than RHA [9].

Aluminium is also used in AFVs. The first generation of aluminium-hulled AFVs (1960s) used the 5083 alloy, whose minor elements are magnesium and manganese. More modern aluminium AFVs use a 7039-type alloy, which contains zinc and magnesium [12]. The latter material has a higher specific strength (see Table 1), but poorer corrosion resistance [13]. Both materials, however, are considerably weaker than RHA. To provide the same level of protection, therefore, the plates need to be thicker than RHA or HHA. One consequence of the increased plate thickness is greater resistance to bending, which means that aluminium-hulled AFVs can often dispense with the stiffening elements common in steel-hulled AFVs [12].

Newer processing techniques such as friction stir processing have been shown to improve the ballistic performance of the high-strength aluminium alloy by introducing hard ceramic particles to the surface of the alloy, creating a composite material on the surface [14].

The other metal used occasionally for armour is titanium, alloys of which are stronger than aluminium but less dense than steel (Table 1). This gives a high specific strength compared to steel and aluminium competitor materials. Although it is an effective armour material, its high price renders it unsuitable for most AFVs [12] [9], nevertheless, it is used in some aircraft (especially ground-attack aircraft which are vulnerable to small-arms fire), where weight is a more important consideration.

Non-metallic armour usually refers to composite materials or ceramics. Composites have the advantage of a relatively low density and an ability to dissipate the energy of incoming projectiles (energy absorption), while ceramic materials make use of their high hardness and compressive strengths (energy disruption). Some ceramic materials in use for armour purposes are boron carbide (B_4C), silicon carbide (SiC) and titanium di-boride (TiB_2) [15]. A detailed overview of such materials, their applications, advantages and disadvantages is given by Hazell [16]. Despite the advantages conveyed by ceramics and composite multilayers, however, the use of such materials remains confined to more specialised and expensive vehicles. Steel armours continue to be used for the majority of AFVs, as they offer protection with a large degree of cost efficiency [17] [18].

3. Defeat mechanisms and projectile behaviour

In this section, we consider projectile impact and different defeat mechanisms under three different categories or regimes: (i) low-speed penetration, where the projectile does not deform significantly; (ii) high speed penetration, where there is extensive plastic deformation of the projectile (the elastic contribution is not the first-order effect and the projectile and target

behave in a fluid-like manner, and are considered as a hydrodynamic interaction); and (iii) spalling, where the projectile is arrested by the armour system but fragments of the armour material are ejected into the vehicle at significant velocities. While projectile penetration of the vehicle does not necessarily occur in the latter, the fragments may still cause significant damage.

3.1 Penetration—Low-speed

Small-arms ammunition includes calibres up to 20 mm [19]. Small-arms ammunition is generally fired at velocities of 600 to 1000 m/s [4]. Two sample experimental studies that investigate these impacts are [20] and [21]. Key factors which influence the nature of the damage and whether penetration will occur are: (i) projectile velocity, (ii) projectile material, (iii) projectile nose shape, (iv) armour type/thickness and (v) armour material.

A vital parameter for any weapon-target combination is the so-called 'ballistic limit' velocity, which marks a 'threshold' velocity above which penetration will occur [4]. Accordingly, and unlike the theory of hydrodynamic penetration (discussed below), the initial projectile velocity is always a crucial factor. There are several ways in which armoured targets can be penetrated, depending on the parameters listed above, and this is illustrated in Fig. 1.

The thickness of the armour plate is a key variable controlling mode of penetration. Thick plates tend to fail by the methods shown in Fig. 1 a) to e), whereas thinner plates tend to bend and stretch around the area of impact (see Fig. 1 f) and Fig. 2), thus absorbing much of the kinetic energy of the projectile [4]. In this way, thinner plates can be more effective per unit mass at stopping projectiles than thicker ones. This means that spaced armour consisting of multiple layers of thinner plates offset from one another can be a mass-effective means of protection. However, this has the disadvantage of adding width and greater geometric complexity to a vehicle hull. Dishing is a failure mechanism evident in thin plates [22] in which

the impact causes a global bending of the plate as well as a local indentation or perforation [23]. Fig. 2 shows the effect of transitioning from dishing (thin plates) to ductile hole enlargement (thicker plates). Iqbal et al [24] carried out a numerical study which demonstrated that sharper-nose projectiles tend to cause failure through ductile hole enlargement (Fig. 1b), while blunter projectiles tended to cause failure through plugging (shear). This is an important consideration, as many studies focus on target response to blunt projectiles (Fig. 1d). Yunfei et al [25] demonstrated experimentally that ductile hole enlargement causes the target material to deform radially, forming a distinctive bulge (see Fig. 2).

Petalling is the phenomenon of radial cracks causing distinctive ‘petals’ of deformed metal on the penetrated rear surface of the target (Fig. 1f). For plates of a moderate thickness, Wei et al [26] showed that shear plugging dominates. For plugging (Fig. 1d), an important mechanism is adiabatic shear fracture [8], where intense heat is generated during the impact event. Because of the short timescales involved, the heat cannot be conducted away and the material temperature rises, thus diminishing its strength [15]. Masri [27] showed that this effect is more pronounced when the target is thin enough to deform in a ductile hole enlargement mode, but not so thin as to fail by dishing. Discing is another failure mechanism in which a region of very high radial strain causes a circumferential crack leading to the complete separation of a ‘disc’ of material from the rear face of the target [28]. Rosenberg and Dekel [4] note that discing is a tensile failure phenomenon and highlight the results by Wingrove [29], showing that projectiles with an ogive-shaped nose tend to cause this effect in high-strength materials. The ogive is the familiar ‘bullet’ shape. The main material component of most small arms projectiles is the lead core. Sometimes steel is used instead of lead as a core material in order to reduce costs. Military small arms ammunition must have a jacket covering the tip of the round—this was specified in the Hague Convention of 1899 [30]. This jacket is generally made from copper alloy or steel.

Other materials can be found inside specialised rounds. For example, 12.7 mm armour-piercing ammunition has a core made from tungsten carbide [31].

Clearly there are a wide variety of materials present in even the simpler forms of anti-armour ammunition. Each of these materials must be modelled accurately in any numerical or theoretical analysis of armour impact events.

3.2 Penetration—high-speed hydrodynamic

The theory of hydrodynamic penetration applies in the case of impact events involving velocities greater than a specific 'transition' velocity, generally greater than 1 km/s [15]. This includes the ordnance range of velocities, variously defined as 1.4 to 1.8 km/s [32], 1.5 km/s [33] [34] [35] and <2.3 km/s [36]; these studies all concern kinetic energy projectiles. The theory, in essence, treats both the target and projectile materials as fluids, neglecting their strengths as the pressure exerted by the projectile is orders of magnitude greater than typical armour strengths [37]. Hydrodynamic penetration theory has also been shown to be applicable to the impact of shaped charge jets, which travel at speeds of 2.5 km/s to 10 km/s [38] (Li et al report on a value of ~6.5 km/s [39] and Jia et al [40] use 4 km/s in their study). An explosively formed projectile travels at comparable but slightly lower speeds: Li et al [41] use speeds of roughly 2900 m/s, while Wu et al [42] operate with speeds of approximately 1500 m/s.

Shaped charge jets are the penetrating mechanism used by most anti-armour munitions, generally taking the form of high-explosive anti-tank (HEAT) rounds [43]. The modern discovery of the shaped charge munition is generally attributed to Charles Munroe in 1888 [44]. Munroe observed that an imprint in a block of explosive was reflected on an adjacent piece of steel after detonation. The imprinted letters created an accelerating jet of material, increasing the penetrating capability of the explosive.

A shaped charge uses the same principle and consists of a cylinder of explosive into which a cone-shaped cavity has been cut, the apex of the cavity facing away from the target. The cavity in the explosive can be lined with metal or unlined. The shaped charge jet consists of the liner material and travels at speeds of many kilometres per second, having very good penetration characteristics. For example, Jia et al [40] studied a standard shaped charge of diameter 56 mm, which could penetrate up to 160 mm of RHA.

A variant of the shaped charge weapon is the explosively formed penetrator/projectile (EFP). This utilises the Misznay-Schardin effect, which is a characteristic of flat sheets or discs of explosive material. When detonated, the explosive blast expands in the direction perpendicular to the plane of the explosive [45]. An EFP consists of a specially-shaped charge of high explosive placed next to a shallow plate of metal, forming it into a quickly-moving projectile upon detonation [46]. EFPs are projected towards their targets at speeds of roughly 2 km/s [4], and are formed from the same material as the munition metal plate. Tantalum is one of the most effective choices, because of its high density and ductility at high strain rates [47]. In their physical characteristics, EFPs differ from shaped charges in that the strains and strain rates involved in forming them are smaller (strain rates not exceeding 10^4 s^{-1}, and true strain $\leq$ 4, compared to strain rates between 10^4 and 10^5 s^{-1} for shaped charges, and true strains of ~10) [48]. In their effects, EFPs tend to be more lethal since they have a larger diameter than shaped charges, causing a wider impact crater and more fragmentation and spalling [4].

Another projectile type which travels at speeds on the hydrodynamic scale is the ‘long rod penetrator’. This is a type of kinetic energy warhead (i.e. it is inert) with a small cross-section and high muzzle velocity, which ensures impact at velocities above the hydrodynamic transition [4], [49]. The high density (they are often made from materials such as tungsten or depleted uranium) [4] and small cross-sectional area of such projectiles maximize penetrative energy on the target. Long-rod penetrators are the main ammunition of most modern main

battle tanks (MBTs), and are referred to by acronyms based on their properties, e.g. APFSDS-T (Armour Piercing Fin-Stabilised Discarding Sabot, Tracer) [50], [43].

Although hydrodynamic penetration is quite common and well-studied, as is low-speed 'rigid' penetration, the transition zone between the two is not well understood. Lou et al [51] attribute this to the complex deformations of the rigid projectile at higher speeds, making it difficult to apply the analytical framework of lower speed impacts. Penetrator erosion, which is the basis for hydrodynamic theory, does not begin to occur until the impact velocity of the projectile exceeds the plastic wave speed of the target [52].

3.3 No penetration—spalling

In some instances, it is possible to defeat an AFV even when full penetration of the armour does not occur. Spalling is a failure mechanism associated with impact, whereby material (from the armour system) is ejected at high velocity. This can cause significant damage or loss of life. Spalling is caused by the interaction of shock waves, which creates a region of high tension within a component [53]. These wave interactions arise when a compression pulse, caused by a high-rate impact on one surface of a body, propagate through the body and then reflect as tensile waves off the far, stress-free surface of the body. The tensile stress field develops at a very high rate, with typical strain rates in the region of 10^4 to 10^6 s^{-1} [53]. This tension field causes the nucleation, growth and coalescence of microscopic voids in the material [54], which leads to fracture and acceleration of fragments from the free end of the body (i.e. the side opposite to the impact surface). Spalling, also referred to as 'scabbing', can be thought of as failure due to cavitation resulting from excessive tensile stresses within the material [55]. Two different kinds of spalling are shown in Fig. 3, one in which a large and intact segment of armour is detached, the other in which many small particles are generated. Whether spalling occurs in a component depends on the tensile strength of the material and the velocity of the

interacting shock waves, which depends on the velocity of the projectile. This is discussed further in Section 4.3. Chen et al [54] observed spall at impact velocities of 129 m/s to 500 m/s. Vogler & Clayton [56] observed that spall severity increases with increasing impact velocity, from 250 m/s to 450 m/s.

The phenomenon of material spallation is best understood from a shock physics perspective, and a comprehensive introduction to the topic is given by Carlucci and Jacobsen [15]. Even without full penetration of armour from an anti-tank weapon, spall fragments can be lethal to vehicle crews. Some armaments, such as high-explosive squash head (HESH) ammunition [57], are designed specifically to maximise pressure waves and spall fragmentation, rather than for penetration of the armour. Spalling is also of interest in the design and protection of structures using cementitious materials, e.g. concrete structures subjected to air blast detonation [58], although the focus of this review is on ductile metal scenarios.

4. Experimental techniques

Experimental techniques are discussed for both low and high-speed tests; the methods examined include both material tests and performance testing of armour systems. Finally, particular attention is given to experimental methods which induce spalling, given its importance in the efficacy of vehicle armour systems.

4.1 Low-speed impact and material testing

Drop testing is perhaps the simplest form of impact mechanics experiment. The projectile is held directly above the target and released, with gravity providing the energy of the impact. A simple and typical methodology for a drop test is described by Aryaei et al [59]. Drop testing is often used for low velocity impacts [60], but limitations on the maximum velocities obtainable give it limited use in the field of terminal ballistics. A drop testing experimental methodology is used by Antoinat et al [61], for example, to investigate the perforation of thin

aluminium plates, but this is only applicable to thin targets. The maximum striking velocity in this case is under 10 m/s [61]. Drop testing can achieve strain rates in the range of 10 to 1000 s^{-1}, which is too low to be relevant for terminal ballistics, apart from rare scenarios as outlined above (strain rates for impact events range from 10^4 to 10^8 s^{-1}) [62].

In order to test the ballistic capabilities of materials, the velocities involved in testing must be similar to the flight velocities of munitions. In 1914 Hopkinson [63] presented a methodology for analysing ballistic impacts. In his setup, the velocity of an impacting bullet causes a pressure wave in a steel bar when it strikes the end of the bar. The bar is split into two sections, and by carefully varying the ratio of their lengths, it is possible to infer the duration and maximum pressure of the impact event. This methodology was modified by Kolsky [64] in 1949 to allow for the measurement of dynamic stress-strain response in specimens contained within a split section of the pressure bar. A schematic and explanation of this method is shown in Fig. 4, and is explained further by Bobbili et al [65]. The striker hits the incident bar, sending a stress wave towards the specimen. Once the stress wave reaches the end of the incident bar, a portion of this wave is transmitted through the specimen to the transmitter bar, while the remainder reflects off the specimen and travels back towards the striker. By instrumenting both bars with strain gauges, the magnitude of the stress waves can be calculated and thus the stress in the specimen inferred. The stain in the specimen is assumed to be uniform and is inferred from the strain in the bars.

The Taylor impact test simply involves firing a cylindrical specimen of test material at a large, rigid, stationary anvil and measurement of the subsequent plastic deformation of the cylinder in order to quantify the material's dynamic yield stress [66]. The test dates from 1946, and although more accurate methods have since been developed, the Taylor test remains useful as a benchmark for material models used in FEA [67]. The main advantage of the Taylor test

is its ability to characterise materials at strain rates of 10^4 to 10^6 s^{-1} using one simple, uniform and easily repeatable test [66].

The test methods mentioned above are shown together in Fig. 5, adapted from a wide-ranging review of experimental impact techniques by Field et al [62], and covering sixteen orders of magnitude of strain rate. However, the focus of the review is firmly towards the right-hand side of the spectrum. At the highest end of Fig. 5 is plate impact. The methodology involved is discussed briefly by Field et al [62] – a disc of material is fired at a target at high speed, producing shock waves in the projectile and target upon impact. A typical velocity for such an experiment is 184 m/s [68]. The loading involved in this kind of impact approximates 1D strain in the initial stages [62]. Impacts of this speed can lead to spallation of the materials, as discussed in greater detail in Section 3.3. At the lower half of Fig. 5, conventional cross-head devices are suitable for experimental purposes. These also have an important role to play in impact mechanics; they can be used alone [69] or in conjunction with higher strain-rate tests [18] as a means of obtaining limited but nevertheless useful empirical data for determining constants in models such as the Johnson-Cook strength model.

4.2 High-speed and ballistic testing

Impacts at higher speeds entail using more elaborate test setups than those described in the previous section. In many cases, full-scale ammunition and weapons are used. A further difficulty arises in the proper instrumentation high-speed testing—the test is pointless if the desired parameter cannot be measured properly. This section discusses the test methods and methods for data and result collection.

NATO STANAG 4659 [6], mentioned in Section 2, defines levels of armour protection. The test procedures for determining performance are outlined in similar detail in STANAG 4164 [70]. These documents describe how to get useful data from test firings of anti-armour

ammunition. NATO define penetration of armour to have occurred (for calibres up to 40 mm) when a hole, through which light is visible, is made in a 'witness plate' (i.e. a plate of thin sheet metal) located behind the target. The US Dept. of the Army [71] define complete penetration in the same way for calibres up to 20 mm. Using a witness plate in this way allows experimental observation of the extent of the behind-armour effects [72]. A second plate can also be placed in front of the target (with a pre-made hole for the projectile to pass through) in order to observe fragmentation on both sides [73].

The simplest form of physical test, of course, is to simply fire an anti-armour weapon or charge at a sample of target material on a firing range (e.g. [50] and [42]). This has the advantage of being the most faithful representation of 'real-life' loading conditions for the armour. On the other hand, there are many variables that cannot be controlled well or at all at such a scale—accuracy of firing and meteorological conditions, for example. For this reason, and because of the cheaper cost and simplicity of setup involved, laboratory gas guns are a common means of testing armour materials [4]. These allow for better control of accuracy and projectile velocity. Schematics of both single-stage and two-stage gas guns are shown in Fig. 6. In the two-stage gas gun, the piston (2) is initiated by combustion of a powder charge in the chamber (7). This rapidly compresses a light gas (e.g. Helium) in the pump tube, bursting the diaphragm (4) at a set pressure and accelerating the projectile (5).

A two-stage gas gun, shown schematically in Fig. 6, can launch a projectile at speeds of up to 10 km/s, as described by Rosenberg & Dekel [4]. A single-stage gas gun is simpler (see Fig. 6), comprising a pressure vessel or powder chamber, a valve and a barrel. Field et al [62] report an upper velocity limit of 1.2 km/s for a single-stage light-gas gun (LGG). Various recent studies with single-stage guns have operated with velocities well below this limit [74], [26], [52], [75]. Two-stage guns, although capable of higher speeds than single ones, are limited with respect to projectile diameter (due to the necessarily smaller diameters in the launch tube)

for an equivalent size and cost of machine [62]. These can be improved even further: for example, Zhao et al [76] report on the case where a two-stage LGG accelerated the projectile up to 7 km/s, and a secondary explosive apparatus attached to the muzzle accelerated it to 10 km/s. Other recent examples of two-stage light gas gun studies may be found in [25], [72], [73].

An important requirement for high-speed impact experiments is the ability to visualise and measure the results. Prentice et al [23] presented a non-contact methodology for measuring displacements of target materials at high strain rates, using high-speed stereoscopic digital speckle photography. Such optical techniques are useful compared to strain gauges, for example, because they provide field rather than point measurement and do not affect the measurement [62]. For further information on the instrumentation of impact experimental techniques, Field et al [62] have conducted an extensive review on the topic.

4.3 Tests for spalling and fragmentation

Since spalling occurs near the free surface, one way to characterise the behaviour of the material is to plot the velocity of that surface as a function of time. This is demonstrated in Fig. 7. The velocity of the impacting projectile is an important parameter, since it directly affects the frequency of the shock wave and thus the free-surface velocity response. Two different responses are shown in Fig. 7, one representing a target material without spalling, and the other one with spalling. The surface velocity of the un-spalled material reduces to near-zero as the pressure wave in the material rebounds. In the spalled material, the mean velocity remains higher, since the detached piece of material is travelling away from the original surface. Knowledge of the free-surface velocity allows for the inference of stress-time history in a material [62].

Practical tests to induce spalling in ductile metals must, due to the nature of the failure mechanism, involve a reasonably complex setup involving a high-speed flyer (projectile), a non-contact means of measuring the velocity of the flyer before impact, and the fitting of certain instrumentation to the target material in order to measure strain response at small time intervals. Fig. 8 shows a typical experimental setup for examining and measuring the phenomenon [53].

The most common and versatile method for obtaining the free-surface velocity data is the velocity interferometer system for any reflector (VISAR) [62], [77]. This technique uses an interferometer to measure the differnece betweeen the optical phase of reflected light from a coherent (i.e. laser) light source which illuminates the surface of interest. The technique, its background, theoretical basis and limitations are described in detail by Dolan [78]. Barker [79] compares VISAR favourably to newer techniques, such as that described by Strand and Whitworth in 2007 [80].

Along with the typical experimental setup, Fig. 8 shows a set of results of such an experiment [53]. These results measured the axial stress as a function of time, for different parallel planes within the material examined (compressive stress on the positive axis). Since spalling is caused by the rapid growth of a tensile stress field, it is clear that this is also an important measure.

Rosenberg and Dekel [4] discuss the difference between full and incipient spall, i.e. the latter consisting of multiple small fragments of material, as opposed to a complete separation of a large fragment, the result of “complete coalescence of the voids, leading to a clear opening inside the specimen" [4]. Deshpande et al [57] also found that the material tends to break up into as many as five pieces in the region close to the axis of the projectile, but with reduced damage closer to the sides, and this has the effect of maintaining material integrity (Fig. 9). It was postulated that the phenomenon of multiple spallation occurs due to the interaction of

multiple waves and their reflections. As the outer free surface of the material detaches due to a stress wave exceeding a critical material tensile strength, a new free surface is created. Stress waves reflect off this new surface and interact with secondary stress waves, causing the growth of voids deeper in the material if the resultant of these waves still exceeds the material strength. This process continues deeper and deeper into the material until the stress waves and their interactions fade in magnitude below the critical material strength [57].

5. Material models

Commonly used constitutive models for various armour materials are presented in the first section and subsequently assessed in terms of their ability to reproduce experimentally observed uniaxial behaviour.

5.1 Constitutive models

A number of different material models have been developed which allow for the calculation of the flow stress of a material being subjected to large strain rates and strains in the plastic region, of which terminal ballistics is an example. Such models are useful in the design and evaluation of armour materials, since they can be used in conjunction with numerical analysis software to accurately predict the response of a material to a given threat. A summary of some of the most widely-used models is given in Table 2.

5.1.1 Johnson-Cook (JC)

One of the most popular constitutive models used in impact situations dates from the 1980s and is known as the Johnson-Cook (JC) model [81]. It takes into account the effects of strain rate and temperature on flow stress:

$$\sigma_{fl} = [A + B\varepsilon^{n}][1 + C \ln \dot{\varepsilon}^{*}][1 - T^{*m}] \quad (1)$$

where ε is the equivalent plastic strain, $\dot{\varepsilon}^*$ is the non-dimensionalised strain rate, T^* is the homologous temperature[1], *A*, *B* and *n* are strain hardening constants, *C* and $\dot{\varepsilon}_0$ (the reference strain rate) are strain rate hardening constants and *m* is a temperature softening constant. Despite its lack of sophistication, this model remains popular as [82]:

- It is easy to understand and implement in FEA codes
- It is intuitive and constants can be approximated without loss of function
- Many existing materials have been characterised by this equation, and their constants are widely available.

Such is the popularity of the JC model that many revisions and additions have been presented over the years; e.g. [83, 84, 85, 86, 87]. For example, Rule & Jones presented a revised form of the model [88] to incorporate two additional empirical constants enhancing the strain rate sensitivity, for higher strain rates, i.e. above 10^4 s^{-1}. The resulting revised Johnson-Cook (RJC) model is:

$$\sigma_{\mathrm{fl}} = [\mathrm{C}_1 + \mathrm{C}_2\varepsilon^{\mathrm{n}}]\left[1 + \mathrm{C}_3 \ln \dot{\varepsilon}^* + \mathrm{C}_4\left(\frac{1}{\mathrm{C}_5 - \ln \dot{\varepsilon}^*} - \frac{1}{\mathrm{C}_5}\right)\right][1 - \mathrm{T}^{*\mathrm{m}}] \qquad (2)$$

The JC model and its variants are the most commonly used methods of analysing experimental results for new or modified armour materials. It is relatively simple to obtain accurate material parameters. For example, Trajkovski et al [69] present a methodology for obtaining JC constants for a new material (PROTAC 500 steel), empirically, through quasi-static temperature-controlled testing.

[1] $T^* = \frac{T}{T_m}$, where T_m is the absolute melting temperature and T is temperature (K).

5.1.2 Zerilli-Armstrong (ZA)

The Zerilli-Armstrong (ZA) model [89] [90] distinguishes between metals with body-centred cubic (BCC) and face-centred cubic (FCC) crystal lattice structures. Pure iron is BCC, although various treatment processes for steels can affect this. Aluminium, on the other hand, is a FCC metal. Table 1 lists some of the materials used for armour purposes. The compact form of the model is described by Meyer [91], which gives the flow stress as:

$$\sigma_{fl} = C_0 + \left(C_1 + C_2\sqrt{\varepsilon}\right)\exp\{-C_3 + C_4 \ln \dot{\varepsilon}\}T + C_5\varepsilon^n \qquad (3)$$

where C_0, C_1, C_2, C_3, C_4, C_5 and n are material constants. For FCC metals $C_1 = C_5 = 0$, whereas for BCC metals $C_2 = 0$. A modified version of the flow stress is presented by Meyer [91] for hexagonal close-packed (HCP) metals, such as Ti-6Al-4V, and is given as

$$\sigma_{fl} = C_0 + C_1 \exp\{-\beta T\} + C_2[\varepsilon_r(1 - \exp\{-\varepsilon/\varepsilon_r\})]\exp\{-\alpha T\} \qquad (4)$$

where

$$\beta = \beta_0\left[1 - \frac{\ln \dot{\varepsilon}}{\ln \dot{\varepsilon}_\beta}\right] \qquad (5)$$

and

$$\alpha = \alpha_0\left[1 - \frac{\ln \dot{\varepsilon}}{\ln \dot{\varepsilon}_\alpha}\right] \qquad (6)$$

where ε_r is a reference strain, and C_0, C_1, C_2, β_0, α_0, $\dot{\varepsilon}_\beta$ and $\dot{\varepsilon}_\alpha$ are material constants. This formulation for the ZA model is used below in Section 5.2.1.

Xu and Huang [92] compare the ZA model to six other constitutive models for experiments on pure copper, finding that it had the highest errors with respect to the

experimental data. It did, however, require the determination of the least number of material parameters (four, compared to nine for a different model), which is an important advantage.

5.1.3 Tanimura-Mimura (TM 2009)

The consititutive model developed by Tanimura and Mimura also differentiates between different materials based on their crystal structure, like the ZA model. The latest iteration of this model, presented in 2009, is known as the TM 2009 model [90], and has the following form for the flow stress:

$$\sigma_{fl} = \sigma_s + \left[\alpha \cdot \left(\varepsilon_p\right)^{m_1} + \beta\right] \cdot \left(1 - \frac{\sigma_s}{\sigma_{CR}}\right) \cdot \ln\left(\frac{\dot{\varepsilon}_p}{\dot{\varepsilon}_{sp}}\right) + B\left(\varepsilon_p\right)\left(\frac{\dot{\varepsilon}_p}{\dot{\varepsilon}_{uni}}\right)^{m_2} \quad (7)$$

where $\dot{\varepsilon}_{sp}$ is the lower limit of the strain rate, $\dot{\varepsilon}_p$ is the plastic strain rate and $\dot{\varepsilon}_{uni}$ is a unit strain rate. The term σ_s is the stress at the lower strain rate $\dot{\varepsilon}_{sp}$, and α, β, σ_{CR}, m_1, m_2 and B are material parameters. The authors of this model found that it matched experimental data much closer than the JC and ZA models, although these results related to vehicle crushing data, rather than ballistic impact, and so involved significantly lower strain rates (1 s^{-1} to 10^3 s^{-1}). Another advantage of the TM 2009 model is that, although there is a large number of material parameters, many of these are constant across an entire material group (e.g. ferrous metal). Because of this, the only information required for a material is the quasi-static stress-strain curve. The model described in Eqn. 7 does not contain a temperature term—the results given in [90] do not mention or account for material temperatures.

5.1.4 Khan-Huang-Liang (KHL)

The modified Khan-Huang-Liang (KHL) model [93] was developed based on experiments carried out on a range of titanium alloys, notably Ti-6Al-4V. The form of the model is

$$\sigma_{fl} = \left[A + B\left(1 - \frac{\ln \dot{\varepsilon}}{\ln D_0^p}\right)^{n_1} (\varepsilon^p)^{n_0}\right]\left(\frac{\dot{\varepsilon}}{\dot{\varepsilon}^*}\right)^C \left(\frac{T_m - T}{T_m - T_r}\right)^m \quad (8)$$

where $\boldsymbol{\varepsilon}^p$ is the plastic strain, $\dot{\varepsilon}$, $\dot{\varepsilon}^*$ are the current strain rate and reference strain rate, similar to the JC model (Eqn. 1), and T_r is a reference temperature. The parameter D_0^p is an arbitrary strain rate, chosen in [93] as 10^6 s^{-1}. The constants *A, B, n_1, n_0, C* and *m* depend on the material. This model was found to correlate better than the JC model with experimental data on dynamic (split Hopkinson pressure bar) impact of Ti-6Al-4V. The effects of thermal softening and a reduction in work hardening at high strain rates are captured by the KHL model.

5.1.5 Physical Base (PB)

The Physical Base (PB) model is explained by Klepaczko et al [94], and also described by Nemat-Nasser, Guo and Isaacs [95], [96], [97]. It developed from observations reported by Seeger [98]. It breaks the total stress into two contributions, an athermal component, which is independent of temperature and strain rate, and a thermally activated second component which takes these factors into account. The rationale behind this approach is explained well by Voyiadjis & Abed [99]. The flow stress takes the form

$$\sigma_{fl} = \sigma_a + \sigma^* \quad (9)$$

where σ_a is the athermal part and σ^* is the thermally activated component, giving a total equivalent stress σ. A power-law approximation gives σ_a:

$$\sigma_a = a_1\left(\bar{\varepsilon}_p\right)^{n_1} \quad (10)$$

In Eqn. 10, $\bar{\varepsilon}_p$ is the plastic strain, a_1 is a material constant and n_1 is a strain hardening exponent. The second part of Eqn. 9 is given as

$$\sigma^* = \hat{\sigma}\left[1 - \left(-\frac{kT}{G_0}\ln\frac{\dot{\bar{\varepsilon}}_p}{\dot{\varepsilon}_r}\right)^{\frac{1}{q}}\right]\left(\frac{1}{p}\right) \tag{11}$$

where $\hat{\sigma}$ is a thermally activated threshold strength, k/G_0 is a ratio characterising the sensitivity of the material to temperature effects (in terms of the reference Gibbs energy at a temperature of absolute zero G_0 and Boltzmann's constant k), $\dot{\varepsilon}_r$ is a characteristic strain rate and p and q are material constants.

5.1.6 Nemat-Nasser & Li (NNL)

The model developed by Nemat-Nasser and Li (NNL) [100] is also physically-based and also breaks the flow stress into thermal and athermal components, as in the PB model. The physical basis for this distinction is based on the barriers to dislocation motion. Short-range barriers such as vacancies, self-interstitials, interstitials and substitutionals caused by alloying elements can be overcome by thermal activation, whereas long-range barriers such as grain boundaries cannot and are therefore athermal [100]. The model developed (this example is based on OFHC[2] copper, a FCC metal) is:

$$\sigma_{fl} = \sigma_0\left\{1 - \left(-\frac{kT}{G_0}\left(\ln\frac{\dot{\varepsilon}}{\dot{\varepsilon}_0} + \ln(1 + a(T)\varepsilon^{0.5})\right)\right)^{0.5}\right\}^{1.5}(1 + a(T)\varepsilon^{0.5}) + \sigma_a^0\varepsilon^{n_1} \tag{12}$$

where

$$a(T) = a_0(1 - (T/T_m)^2) \tag{13}$$

[2] Oxygen-free high [thermal] conductivity

In the model above, a_0 is a constant reflecting the initial average dislocation spacing, k/G_0 is the ratio of the Bolzmann constant to the Gibbs energy and has units of K^{-1}, $\dot{\varepsilon}_0$ is a reference strain rate, σ_0 is a characteristic thermally activated stress, σ_a^0 is a characteristic athermal stress and n_1 is a material-dependent exponent. It was found it to be in good agreement with split Hopkinson bar experimental results over temperatures of 77 to 1100 K, strain rates of 10^{-3} to 8000 s^{-1} and strains of greater than 100% [100].

5.1.7 Rusinek-Klepaczko (RK)

Rusinek and Klepaczko [94], [101] presented a model which, in a similar manner to the PB model above, is based on the addition of athermal and thermally activated stresses:

$$\sigma_{fl} = \frac{E(T)}{E_0}\left[B\left(\dot{\bar{\varepsilon}}_p, T\right)\left(\varepsilon_0 + \bar{\varepsilon}_p\right)^{n\left(\dot{\bar{\varepsilon}}_p, T\right)} + \sigma_0^* \langle 1 - D_1 \left(\frac{T}{T_m}\right) \log\left(\frac{\dot{\varepsilon}_{max}}{\dot{\bar{\varepsilon}}_p}\right)\rangle^{m^*}\right] \tag{14}$$

The Macaulay operator sets the expression inside the brackets to zero if it is less than zero, thus eliminating the instantaneous rate sensitivity of the model at high temperatures and low strain rates [94]. The elastic modulus, plastic modulus and strain hardening exponent functions are:

$$E(T) = E_0\left\{1 - \frac{T}{T_m}\exp\left[\theta^*\left(1 - \frac{T_m}{T}\right)\right]\right\} \tag{15}$$

$$B\left(\dot{\bar{\varepsilon}}_p, T\right) = B_0\left(\left(\frac{T}{T_m}\right)\log\left(\frac{\dot{\varepsilon}_{max}}{\dot{\bar{\varepsilon}}_p}\right)\right)^{-\nu} \tag{16}$$

$$n\left(\dot{\bar{\varepsilon}}_p, T\right) = n_0\left\{1 - D_2\left(\frac{T}{T_m}\right)\log\frac{\dot{\bar{\varepsilon}}_p}{\dot{\varepsilon}_{min}}\right\} \quad , \quad n \geq 0 \tag{17}$$

E_0 is the Young's modulus at T = 0 K, θ^* is the characteristic homologous temperature of the material (a material constant, $\theta^* \approx 0.5$ for ferritic steels), $\boldsymbol{\varepsilon_0}$ is the strain at yield in quasi-

static loading, σ_0^* is the effective stress at T = 0 K, D_1 is a material constant, $\dot{\varepsilon}_{min}$ and $\dot{\varepsilon}_{max}$ are the limits for strain rates in the model, m^* is a strain rate temperature dependency constant, B_0 is a material constant modulus of plasticity, D_2 is a material constant, and all other symbols have the same meanings as in previous models. A modified version of the RK model was presented in [102], with a specific application to FCC metals, namely copper.

5.1.8 Voyiadjis-Abed (VA)

The Voyiadjiz-Abed (VA) model, in a similar way to the ZA model, also distinguishes between BCC and FCC metals, and is physically-based, with flow stress split into thermally activated and athermal components. The equation for the flow stress of BCC metals is given as

$$\sigma_{fl} = \hat{Y}\left(1 - \left(\beta_1 T - \beta_2 T \ln \dot{\varepsilon}_p\right)^{1/q}\right)^{1/p} + B\varepsilon_p^n + Y_a \qquad (18)$$

where Y_a is the initial athermal yield stress, $\hat{Y}$ is the threshold yield stress of the Peierls barrier to dislocation motion, p and q are material constants ($0 \leq p \leq 1.0$, $1.0 \leq q \leq 2.0$), β_1 and β_2 are material parameters, B is a hardening constant and n is a material exponent. For FCC metals, the flow stress is

$$\sigma_{fl} = B\varepsilon_p^n\left(1 - \left(\beta_1 T - \beta_2 T \ln \dot{\varepsilon}_p\right)^{1/q}\right)^{1/p} + Y_a \qquad (19)$$

and all the symbols have the same definitions as in Eqn. 18.

5.2 Comparison of Strength Models

It is of interest to explore the relative performance of these material models. Hence, some of the key models discussed above are compared here for uniaxial conditions based on available published values for material constants. The material chosen for the purposes of comparison was Ti-6Al-4V, since it is one of the better characterised materials. The three models compared

were the Johnson-Cook (JC), Zerilli-Armstrong (ZA) and Khan-Huang-Liang (KHL) models. The material parameters and their sources are presented in Table 3.

The data in Table 3 were used to predict the uniaxial tensile stress-strain response for each material at a range of temperatures and strain rates and compared with experimental results on the same material, as presented by Chen et al. [103]. The results of this analysis are shown in Fig. 10.

The results presented span a wide range of strain-rates (1×10^{-4} to 1×10^{4} s^{-1}) and temperatures (room temperature and 700° C). At room temperature and 1×10^{-4} s^{-1}, the JC and KHL models both perform well, whereas the ZA model significantly overpredicts stress for low strain (< 0.15) and underpredicts it for higher strains. At a higher strain rate of 1×10^{-2} s^{-1}, the JC and KHL models again show good correlation to the test data at both temperatures, although they slightly overpredict stress at room temperature and show too much hardening at higher strains at the higher temperature. The ZA model again performs relatively poorly at room temperature, overpredicting stress for yield and low strains and underpredicting for higher strains; this model shows negligible hardening, but captures the mean stress reasonably well overall. For the much larger strain rate of 2500 s^{-1}, all three models overpredict stress at both temperatures, most significantly at yield and lower strains. Both the JC and the KHL models perform well at the higher strains for 700° C. At the highest strain rate of 1×10^{4} s^{-1}, all three models overpredict stress, particularly (i.e. by 30% to 50%) at yield and low strain for room temperature, but perform significantly better at higher strains. At 700° C, for this rate, the JC and KHL models significantly overpredict hardening (and hence stress) at moderate to high strains (>0.05); the KHL model gives closer results to the test data, however.

In some cases, the ZA model results are not shown at the higher temperature due to extremely high (apparently non-physical) stress levels. Meyer modified the ZA model to capture the behaviour of HCP materials such as Ti-6Al-4V. However, Meyer considered a wide

range of strain rates, up to 4.64 x 10^4 s^{-1}, and the original calibration also performed poorly at strain rates below 2.20 x 10^4 s^{-1}. Xu and Huang [92], who carried out tests on OFHC Cu reached the same conclusion for the ZA model with FCC materials. In summary, based on the data in Fig. 10, the ZA is considered to be the least accurate of the models analysed, showing the greatest departure from the experimental data. Of the other two models, KHL is marginally closer to a full agreement with the experimental data than the JC model, although the former requires an additional two material constants compared to the latter.

6. Numerical considerations

6.1 Analysis Codes used

Due to the complex nature of the dynamic loading, geometry and boundary conditions inherent in impact mechanics with application to ballistics, very few problems which have a practical application are amenable to analytical solution. Thus, simulation of these impact events generally requires advanced numerical techniques. Rosenberg & Dekel [4] discuss the advantages of finite element (FE) and finite difference methods in ballistic 'hydrocode' simulations where they also explain the relative merits of Lagrangian versus Eulerian analysis techniques. Lagrangian analyses couple the material points on the deforming solid to the nodes of the mesh, whereas the Eulerian approach fixes the mesh as an unchanging reference frame and allows material points and surfaces to deform within that mesh. A more detailed explanation of both is given by Donea et al. [104]. It is concluded that an ideal compromise in a ballistics simulation is to model the projectile in a Lagrangian mesh (assuming it to be hard and non-deforming) and the target in a Eulerian grid (assuming it to be softer and deforming) [4].

Another way of achieving the advantages of a Lagrangian approach whilst allowing for large deformation is through the use of smooth particle hydrodynamics (SPH) [105]. The

application of this computational method to impact problems began in the early 1990s and initial descriptions, algorithms and examples are presented by [106], [107], [108]. It has now been implemented in commercial FE codes such as Abaqus and Ansys.

Johnson et al [109] conducted an early review of the application of SPH to ballistics problems. A number of algorithms and examples were presented, with the long-term goal of developing a method in which a standard Lagrangian finite element grid could be drawn for any impact problem, with the code automatically changing highly deformed elements of the material to SPH nodes [109]. In subsequent work, Johnson [82] presented examples of simulations where this had been achieved, thus demonstrating the value of linking FE and SPH methods. A further advantage of the mesh-free nature of SPH, as explained by Batra & Zhang [110], relates to the simulation of crack propagation which is more realistic, as it is dictated by physics and not the location and density of the mesh at any particular point.

The popularity of four major numerical codes over the past 25 years is shown in Fig. 11. The results are based on a search of keywords in a leading journal of impact mechanics, and the codes considered are EPIC [111], [82]; Ansys AUTODYN [112]; Abaqus/Explicit [113] and LS-DYNA [114]. This is coupled with a significant growth over the same time period in the use of finite element methods to address problems in impact mechanics. The proportion of articles on impact mechanics which include FEA has increased from less than 10% to nearly 50% of all articles published. In the past 15 years, LS-DYNA and Abaqus/Explicit have supplanted EPIC and, to a lesser extent, Ansys Autodyn as the most popular codes. An example of results from EPIC is shown in Fig. 12. The growth in the level of numerical analysis is reflective of the maturity of the analysis packages and that there is greater confidence in their results as a result of greater comparisons with experimental data. The other significant change is that the growth in computing power has facilitated the analysis of more meaningful problems having greater complexity.

7. Future trends

7.1 Advanced armours

Layered armour is a technique which is gaining in popularity over recent years and is becoming standard with the heaviest and most advanced classes of AFVs [9]. One such example in use by British and US forces is Chobham armour, which is composed of tiles or cells of ceramic materials in a metallic matrix. Although the details of Chobham armour remain classified, there is a wealth of published literature on ceramic armour in general. For example, Hohler et al [115] evaluated a number of ceramic materials in a layered system with metallic plates in order to determine the ideal ceramic and the ideal ratio of ceramic to metallic material. Bürger et al [116] carried out an FEA simulation of a ceramic composite armour, including detail on the brittle material models used in the code. Hogan et al [117] present a detailed experimental analysis of ceramic impact events, measuring the dispersion of spall material.

Sandwiching together materials with different properties is a cost-effective way to optimise armour, as it allows for different layer properties to have varying effects on a projectile as it penetrates [17]. Worsham et al [118] present a novel system of armour (shown in Fig. 13) which uses a number of different layers, each of which is specifically designed to have a different negative effect on a penetrator.

In Corvid's system (Fig. 13), the angled plates of hardened steel break up incoming projectiles and impart a rotation to them, reducing the component of velocity normal to the face of the armour. The aluminium plates serve to hold these hardened steel plates in the correct orientation, especially with multiple impacts. The air gap (in Fig. 13, this is filled with foam) gives space for projectiles and debris to disperse somewhat. The hardened steel plate provides the main armour protection, and the composite materials behind it serve as a spall liner, catching debris and preventing it from entering the crew compartment.

Explosive reactive armour (ERA) was developed specifically to counteract the threat posed by shaped-charge weapons. It consists of a ‘sandwich’ of high-explosive material held between two steel plates. The whole unit is attached to the outside of the AFV’s main armour, with a gap between the main armour and the ERA. When a shaped charge interacts with the explosive the latter detonates, causing the steel plates to accelerate forwards and backwards. The plates interact with the shaped charge jet, moving obliquely and continuously presenting new material which the jet erodes. This serves to diminish the power of the jet and break it up, in turn reducing the penetrating potential it has on the main armour of the vehicle [119]. ERA can reduce the effect of a shaped charge (i.e. the depth of penetration into the main armour) by up to 75%, although the effect is significantly reduced or even eliminated if the impact occurs at right angles [39]. There are multiple disadvantages of ERA, such as:

- Each module of ERA can absorb one strike, after which it is destroyed. Some complex anti-tank warheads exploit this by using a ‘tandem’ warhead with axially stacked shaped charges.
- The fragments of ERA have significant kinetic energy, posing a serious hazard for ground troops in support of AFVs or unprotected non-combatants in the area.
- There is a challenge in designing modules of ERA which can operate as designed without causing adjacent modules to sympathetically detonate. The challenges in creating an effective pattern are discussed by Rosset [120].

More recent developments in this field include attempts to design ERA which will defeat the threat from kinetic energy projectiles (see Section 3.2). As with the defeat of a shaped charge, a lot of the variability in the performance of the armour is dependent on the angle of impact, with a more oblique angle producing a better effect [35].

7.2 Vulnerability models

Germany's Universelles Verwundbarkeitsmodell (Universal Vulnerability Model, shortened to UniVeMo) is used by the German Army as the standard for predicting the lethality of weapons and the vulnerability of vehicles, structures and troops [121] [122]. Rather than simulating only one specific impact event in isolation, this model tries to quantify the global effects of anti-armour weapons on vehicles and troops and ultimately on the force's combat effectiveness. An earlier incarnation of the model was presented by Arnold and Paul [123], which focused on the behind-armour debris cloud (i.e. spalling) as a continuation of Arnold and Schäfer's work on this topic [72] (see Section 4.2).

The dearth of published material on equivalent vulnerability models for other military forces is not necessarily indicative of their absence, since there are legitimate security considerations for keeping such information under close control. Nevertheless, through the use of improved numerical models and computational resources, such vulnerability models are likely to improve significantly in capability and prevalence in the near future.

7.3 Multi-scale modelling

Techniques for evaluating and simulating the role of microstructure in the response of materials to impact loading are becoming increasingly prevalent. For example, Field et al note that progress has been made in using advanced techniques, coupled with the power of supercomputers, to improve the imaging resolution of VISAR (mentioned in Section 4.3) to observe the motions of individual grains of a material [62]. This is becoming more important as new forming and manufacturing techniques for improved armours involve more careful control of material microstructures. For example, Wielewski et al [124] hypothesise a method for improving the spall strength of Ti-6Al-4V based on careful control of certain microstructural features of the material, such as the number of plastically hard or soft grain

boundaries. Hazell et al [125] subjected Elektron 675, a magnesium alloy, to a number of spall experiments. It was found that long striations of small grains, which formed along the extrusion direction of the material, provided an opportunity for cracks to grow at right angles to the spall plane.

Barrett et al [126], Golden et al [127] and Li et al [128] developed a multiscale viscoplastic model of P91 steel, incorporating it into the macro-scale FEA analyses using a representative volume element (RVE). A schematic representation of the complex grain structure of this material is shown in Fig. 14. The hierarchical grain structure with strengthening mechanisms shown in Fig. 14, although taken from a study on cyclic viscoplasticity in chrome steels with small strain ranges [126], is a useful example of the kind of microstructural considerations which would feed into a multiscale model for ballistic impact. Jacques et al [129] presented a finite-element model which incorporates the role of micro-inertial effects due to void growth for ductile fracture. Their models take account of void nucleation and growth by modelling such voids within a larger RVE—the formulation of this is also discussed in greater detail by Sartori et al [130] and Molinari & Mercier [131]. The RVE contains a number of spherical voids of varying radii embedded in spherical shells of matrix material. In a comprehensive review of their work in this field [132], the authors explain the relationship between the macro (component) level, the mesoscopic level, in which an RVE is constructed for each integration point on the macro level, and the micro level, which consists of a single void. The behaviour of the unit cells and RVEs was governed by an analytical relationship which was verified by FEA calculations at the void level. The work carried out by Jacques, Mercier, Molinari and Sartori related to plate impact tests on tantalum; the results [133] showed a very good correlation between experimental data and the micro and macro level model. If such methods could be extended to a general class of metallic materials, this would facilitate the development of a material design tool for terminal ballistics, in which

microstructural variables, instead of empirically-derived coefficients, could be used to predict and therefore optimise material performance.

7.4 Material design tool

A recent study [134] analysed a wealth of experimental data for a range of materials to develop a powerful means of predicting ballistic limit velocities and penetration thicknesses. It was also noted, however, that it should soon be possible to predict these quantities from information regarding material chemistry and heat treatment alone.

Rusinek at al [102] distinguish between phenomenological (i.e. empirical) material models and physically-based models. While the former, if implemented correctly, can have fewer material constants, they suffer from lack of applicability and flexibility. The latter are more universal and have greater flexibility, but require a large number of material constants. They can provide more accurate results: Fig. 15 demonstrates the accuracy of the RK model, described in Section 5.1.7, when compared with experimental data. Although the materials used in Fig. 10 and Fig. 15 are different, the better agreement with experimental data in the latter example is obvious.

A micromechanical model, i.e. one which was based on a fundamental analysis of the physical activity at the grain and crystal scale, would in theory allow for the useful generality of the physically-based model with the simplicity of the phenomenological model. Nemat-Nasser and Li referred to these micromechanical models in 1998 [100], pointing out that such models always require some degree of empirical evaluation of certain material parameters in order to be useful. Dunne & Petrinic [135] also mention the challenges inherent in modelling crystal plasticity computationally, although it must be borne in mind that exponential improvements in computing power constantly provide new opportunities and impetus for such

research. It is clear that much work remains to be done in this field before adequate material design tools are available.

8. Conclusion

The integrity of vehicular armour is clearly of the utmost importance for designers and military planners. The threat profile facing armoured vehicles is quite diverse and so there are multiple requirements for armour materials.

This review first listed the main categories of material used in vehicular armour, and compared their attributes, strengths and weaknesses. It was found that among metals, specialised steels continue to be the most prevalent material, and metallic armour in general is much more pervasive and widespread than ceramic or composite-based armour. This is mainly due to cost and manufacturability considerations. Following on from that was a summary of the main defeat mechanisms for armoured vehicles. It was shown that with low-speed penetration, a variety of failure mechanisms prevail based on projectile material, geometry and impact speed. Projectiles themselves vary in their size and composition, highlighting the importance of proper material information when doing theoretical or numerical modelling. This kind of modelling must be rigorously tested and 'reality-checked', on account of the variety of failure mechanisms.

With high-speed penetration, a different mode of analysis, one based on fluid hydrodynamics, becomes important. The next section of the review described various experimental techniques in both the low and high-speed testing regions, and charted their popularity over time. It was shown that certain popular impact test methods such as drop testing can be inadequate for the higher strain rates involved in terminal ballistics.

Section 5 explained eight different material constitutive models and compared three in terms of their flexibility and adaptability to different strain, strain rate and temperature regimes.

The results illustrate a challenge which faces designers—the variability of many of the material models. They demonstrate narrow ranges of applicability, outside of which they fail to predict real-life results with sufficient accuracy. Since quasi-static testing is the most practicable way of obtaining stress-strain data from a previously uncharacterised material, this creates a difficulty and makes it difficult to calibrate data. However, quasi-static testing or dynamic testing at lower strain rates is often used to provide material data for these models; either more extensive testing is required or more universal material models must be developed. Without accurate material constants, the usefulness of the numerical methods described in Section 6 is severely limited.

In conclusion, despite the extensive literature reporting experimental data and the many material models available, design of metallic military vehicular armour is a task complicated by the lack of universally applicable material models and the extensive testing and calibration requited for current models. From the designer's perspective, a design tool that describes the response of a variety of metallic armour materials to various impacts is a panacea; such a tool would require only the microscale material structure (for example, grain sizes and crystal structures) and the chemical composition in order to predict material behaviour from the quasi-static to the hypervelocity range. As computational capabilities continuously grow, coupled with more competent material models, this objective becomes a realistic target.

References

[1] E. Greenhalgh, "Technology Development in Coalition: The Case of the First World War Tank," *The International History Review*, vol. 22, no. 4, pp. 806-836, 2000.

[2] A. Ramasamy, S. Harrisson, I. Lasrado and M. P. Stewart, “A review of casualties during the Iraqi insurgency 2006–A British field hospital experience,” *Injury,* vol. 2009, no. 40, pp. 493-497, 2009.

[3] S. J. Wolf, V. S. Bebarta, C. J. Bonnett, P. T. Pons and S. V. Cantrill, “Blast injuries,” *The Lancet,* vol. 2009, no. 374, pp. 405-415, 2009.

[4] Z. Rosenberg and E. Dekel, Terminal Ballistics, New York: Springer, 2012.

[5] K. Maweja and W. Stumpf, “The design of advanced performance high strength low-carbon martensitic armour steels. Part 1. Mechanical property considerations,” *Materials Science and Engineering,* vol. 485, pp. 140-153, 2008.

[6] NATO Military Agency for Standardisation, “STANAG 4569: Protection levels for occupants of logistic and light armour vehicles,” NATO, Brussels.

[7] R. M. Ogorkiewicz, “NATO airs new vehicle protection standards,” *Jane's International Defence Review,* August 2013.

[8] A. Molinari, S. Mercier and N. Jacques, “Dynamic failure of ductile materials,” *Procedia IUTAM,* vol. 10, pp. 201-220, 2014.

[9] P. J. Hazell, “The Development of Armour Materials,” *Military Technology,* vol. 30, no. 4, pp. 54-62, 2006.

[10] P.J.Hazell, M. Edwards, H. Longstaff and J. Erskine, “Penetration of a glass-faced transparent elastomeric resin by a lead-antimony-cored bullet,” *International Journal of Impact Engineering,* vol. 36, no. 1, pp. 147-153, 2009.

[11] E. DeGarmo, Materials and processes in manufacturing, Hoboken, NJ, USA: Wiley, 2003.

[12] R. M. Ogorkiewicz, Technology of Tanks (Volume II), London: Jane's Information Group, 1991.

[13] S. J. Pérez-Bergquist, G. T. R. Gray, E. K. Cerreta, C. P. Trujillo and A. Pérez-Bergquist, "The dynamic and quasi-static mechanical response of three aluminum armor alloys: 5059, 5083 and 7039," *Materials Science and Engineering A,* vol. 528, pp. 8733-8741, 2011.

[14] I. Sudhakar, V. Madhu, G. M. Reddy and K. S. Rao, "Enhancement of wear and ballistic resistance of armour grade AA7075 aluminium alloy using friction stir processing," *Defence Technology,* vol. 11, pp. 10-17, 2015.

[15] D. E. Carlucci and S. S. Jacobson, Ballistics- Theory and Design of Guns and Ammunition, Boca Raton, FL: CRC Press, 2008.

[16] P. J. Hazell, "Advances in Ceramic Armour," *Military Technology,* pp. 118-126, April 2009.

[17] N. Brown, "Lighten up: tracking innovations in passive armour solutions," *Jane's International Defence Review,* vol. 46, no. April, pp. 62-65, 2013.

[18] M. Nilsson, "Constitutive Model for Armox 500T and Armox 600T at Low and Medium Strain Rates," FOI: Swedish Defence Research Agency, Tumba, Sweden, 2003.

[19] Joint Education and Doctrine Division J-7, US Armed Forces, "DOD Dictionary of Military and Associated Terms," 15 March 2015. [Online]. Available: http://www.dtic.mil/doctrine/dod_dictionary/?zoom_query=small+arms. [Accessed 5 May 2015].

[20] T. Børvik, S. Dey and A. H. Clausen, "Perforation resistance of five different high-strength steel plates subjected to small-arms projectiles," *International Journal of Impact Engineering,* vol. 36, pp. 948-964, 2009.

[21] N. Kılıç, S. Bedir, A. Erdik, B. Ekici, A. Taşdemirci and M. Güden, "Ballistic behavior of high hardness perforated armor plates against 7.62 mm armor piercing projectile," *Materials & Design,* vol. 63, pp. 427-438, 2014.

[22] Y. W. Lee and T. Wierzbicki, "Fracture prediction of thin plates under localized impulsive loading. Part I: Dishing," *International Journal of Impact Engineering,* vol. 31, pp. 1253-1276, 2005.

[23] H. J. Prentice, W. G. Proud, S. M. Walley and J. E. Field, "Optical techniques for the investigation of the ballistic impact of thin plates," *International Journal of Impact Engineering,* vol. 38, no. 11, pp. 849-863, 2011.

[24] M. A. Iqbal, G. Gupta, A. Diwakar and N. K. Gupta, "Effect of projectile nose shape on the ballistic resistance of ductile targets," *European Journal of Mechanics, A/Solids,* vol. 29, no. 4, pp. 683-694, 2010.

[25] D. Yunfei, Z. Wei, Y. Yonggang, S. Lizhong and W. Gang, "Experimental investigation on the ballistic performance of double-layered plates subjected to impact by projectile of high strength," *International Journal of Impact Engineering,* vol. 70, pp. 38-49, 2014.

[26] Z. Wei, D. Yunfei, C. Z. Sheng and W. Gang, "Experimental investigation on the ballistic performance of monolithic and layered metal plates subjected to impact by blunt rigid projectiles," *International Journal of Impact Engineering,* vol. 49, pp. 115-129, 2012.

[27] R. Masri, “The effect of adiabatic thermal softening on specific cavitation energy and ductile plate perforation,” *International Journal of Impact Engineering,* vol. 68, pp. 15-27, 2014.

[28] Y. W. Lee and T. Wierzbicki, “Fracture prediction of thin plates under localized impulsive loading. Part II: discing and petalling,” *International Journal of Impact Engineering,* vol. 31, pp. 1277-1308, 2005.

[29] A. L. Wingrove, “The influence of projectile geometry on adiabatic shear and target failure,” *Metallurgical Transactions,* vol. 4, pp. 1829-1833, 1973.

[30] J. B. Scott, *The Hague Peace Conferences of 1899 and 1907: A Series of Lectures Delivered before the Johns Hopkins University in the Year 1908,* Baltimore, MD, USA: The Johns Hopkins Press, 1909.

[31] T. Børvik, S. Dey and L. Olovsson, “Penetration of granular materials by small-arms bullets,” *International Journal of Impact Engineering,* vol. 75, pp. 123-139, 2015.

[32] Z. Rosenberg and E. Dekel, “On the role of material properties in the terminal ballistics of long rods,” *International Journal of Impact Engineering,* vol. 30, pp. 835-851, 2004.

[33] N. Lynch, “Constant kinetic energy impacts of scale size KE projectiles at ordnance and hypervelocity,” *International Journal of Impact Engineering,* vol. 23, pp. 573-584, 1999.

[34] Y. Partom and D. L. Littlefield, “Validation and calibration of a lateral confinement model for long-rod penetration at ordnance and high velocities,” *International Journal of Impact Engineering,* vol. 17, pp. 615-626, 1995.

[35] S. H. Paik, S. J. Kim, Y. H. Yoo and M. Lee, “Protection performance of dual flying oblique plates against a yawed long-rod penetrator,” *International Journal of Impact Engineering,* vol. 34, pp. 1413-1422, 2007.

[36] F. I. Grace, “Ballistic limit velocity for long rods from ordinance velocity through hypervelocity impact,” *International Journal of Impact Engineering,* vol. 23, pp. 295-306, 1999.

[37] C. Anderson and D. Orphal, “An examination of deviations from hydrodynamic penetration theory,” *International Journal of Impact Engineering,* vol. 2008, no. 35, pp. 1386-1392, 2008.

[38] C. Poole, *Penetration of a shaped charge (Diss.),* Oxford: University of Oxford, 2005.

[39] X.-d. Li, Y.-s. Yang and S.-t. Lv, “A numerical study on the disturbance of explosive reactive armors to jet penetration,” *Defence Technology,* vol. 10, no. 1, pp. 66-75, 2014.

[40] X. Jia, Z. X. Huang, X. D. Zu, X. H. Gu and Q. Q. Xiao, “Theoretical analysis of the disturbance of shaped charge jet penetrating a woven fabric rubber composite armor,” *International Journal of Impact Engineering,* vol. 65, pp. 69-78, 2014.

[41] W. Li, X. Wang and W. Li, “The effect of annular multi-point initiation on the formation and penetration of an explosively formed penetrator,” *International Journal of Impact Engineering,* vol. 37, no. 4, pp. 414-424, 2010.

[42] J. Wu and J. D. Y. Liu, “Experimental and numerical study on the flight and penetration properties of explosively-formed projectile,” *International Journal of Impact Engineering,* vol. 34, pp. 1147-1162, 2007.

[43] DCSINT, “OPFOR: Worldwide equipment guide,” Training and Doctrine Command, US Army, Ft. Leavenworth, KS, 1999.

[44] W. Walters, “A brief history of shaped charges,” in *24th International Symposium on Ballistics*, New Orleans, 2008.

[45] J. T. Thurman, Practical Bomb Scene Investigation, 2 Ed., Boca Raton, LA, USA: CRC Press, 2011.

[46] J. Hallquist, G. Goudreau and D. Benson, “Sliding interfaces with contact-impact in large-scale Lagrangian computations,” *Computer Methods in Applied Mechanics and Engineering,* vol. 51, pp. 107-137, 1985.

[47] S. Cardonne, P. Kumar, C. Michaluk and H. Schwartz, “Tantalum and its alloys,” *International Journal of Refractory Metals and Hard Materials,* vol. 13, pp. 187-194, 1995.

[48] L. E. Murr, E. T. Ferreyra, S. Pappu, E. P. Garcia, J. C. Sanchez, W. Huang, J. M. Rivas, C. Kennedy, A. Ayala and C. S. Niou, “Novel deformation processes and microstructures involving ballistic penetrator formation and hypervelocity impact and penetration phenomena,” *Materials Characterization,* vol. 37, no. 96, pp. 245-276, 1996.

[49] H. Shin and W. Lee, “Material design guidelines for explosive confinements to control impact shock-induced detonations based on shock transmission/reflection analysis,” *International Journal of Impact Engineering,* vol. 28, pp. 465-478, 2003.

[50] B. Mishra, P. K. Jena, B. Hazarika, K. Siva Kumar and T. Balakrishna Bhat, “An experimental study on the shattering behavior of a high strength armour steel under blast and long rod penetrator impact,” *Materials and Design,* vol. 31, no. 8, pp. 3971-3981, 2010.

[51] J.-f. Lou, Y.-g. Zhang, Z. Wang, T. Hong, X.-l. Zhang and S.-d. Zhang, “Long-rod penetration: The transition zone between rigid and hydrodynamic penetration modes,” *Defence Technology,* vol. 10, no. 2, pp. 239-244, 2014.

[52] H. N. Krishna Teja Palleti, S. Gurusamy, S. Kumar, R. Soni, B. John, R. Vaidya, A. Bhoge and N. K. Naik, “Ballistic impact performance of metallic targets,” *Materials and Design,* vol. 39, pp. 253-263, 2012.

[53] T. Antoun, D. R. Curran, S. V. Razorenov, L. Seaman, G. I. Kanel, A. V. Utkin and Y. Horie, Spall Fracture, New York: Springer, 2003.

[54] D. Chen, H. Tan, Y. Yu, H. Wang, S. Xie, G. Liu and Z. Yin, “A void coalescence-based spall model,” *International Journal of Impact Engineering,* vol. 2006, no. 32, pp. 1752-1767, 2006.

[55] C. Danian, Y. Yuying, Y. Zhihua, W. Huanran, L. Guoqing and X. Shugang, “A modified Cochran–Banner spall model,” *International Journal of Impact Engineering,* vol. 2005, no. 31, pp. 1106-1118, 2005.

[56] T. Vogler and J. Clayton, “Heterogeneous deformation and spall of an extruded tungsten alloy: plate impact experiments and crystal plasticity modeling,” *Journal of the Mechanics and Physics of Solids,* vol. 2008, no. 56, pp. 297-335, 2008.

[57] P. Deshpande, V. Prabhu and K. Prabhakaran, “Impulsive Loading of Armour by High Explosive Squash Head Munition,” *Defence Science Journal,* vol. 53, no. 4, pp. 357-365, 2003.

[58] J. Li and H. Hao, “Numerical study of concrete spall damage to blast loads,” *International Journal of Impact Engineering,* vol. 2014, no. 68, pp. 41-55, 2014.

[59] A. Aryaei, K. Hashemnia and K. Jafarpur, “Experimental and numerical study of ball size effect on restitution coefficient in low velocity impacts,” *International Journal of Impact Engineering,* vol. 37, no. 10, pp. 1037-1044, 2010.

[60] D. Starratt, T. Sanders, E. Cepuš, A. Poursartip and R. Vaziri, “Efficient method for continuous measurement of projectile motion in ballistic impact experiments,” *International Journal of Impact Engineering,* vol. 24, pp. 155-170, 2000.

[61] L. Antoinat, R. Kubler, J.-L. Barou, P. Viot and L. Barrallier, “Perforation of aluminium alloy thin plates,” *International Journal of Impact Engineering,* vol. 75, pp. 255-267, 2015.

[62] J. E. Field, S. M. Walley, W. G. Proud, H. T. Goldrein and C. R. Siviour, “Review of experimental techniques for high rate deformation and shock studies,” *International Journal of Impact Engineering,* vol. 30, pp. 725-775, 2004.

[63] B. Hopkinson, “A Method of Measuring the Pressure Produced in the Detonation of High Explosives or by the Impact of Bullets,” *Philosophical Transactions of the Royal Society of London,* pp. 411-413, 1914.

[64] H. Kolsky, “An investigation of the mechanical properties of materials at very high rates of loading,” *Proceedings of the Physical Society,* vol. 62, pp. 676-700, 1949.

[65] R. Bobbili, B. Ramakrishna, V. Madhu and A. Gogia, “Prediction of flow stress of 7017 aluminium alloy under high strain rate compression at elevated temperatures,” *Defence Technology,* vol. 11, no. 1, pp. 93-98, 2015.

[66] D. J. Chapman, D. D. Radford and S. M. Walley, “A History of the Taylor Test and Its Present Use in the Study of Lightweight Materials,” *Design and Use of Light-Weight Materials,* pp. 12-24, 2005.

[67] L. Forde, W. Proud and S. Walley, “Symmetrical Taylor impact studies of copper,” *Proceedings of the Royal Society A: Mathematical, Physical and Engineering Sciences,* vol. 465, pp. 769-790, 2009.

[68] W. Tong, “Pressure-shear stress wave analysis in plate impact experiments,” *International Journal of Impact Engineering,* vol. 19, no. 2, pp. 147-164, 1997.

[69] J. Trajkovski, R. Kunc, V. Pepel and I. Prebil, “Flow and fracture behavior of high-strength armor steel PROTAC 500,” *Materials & Design,* vol. 66, pp. 37-45, 2015.

[70] NATO Military Agency for Standardisation, *STANAG 4164 Land (Edition 2)- Test Procedures for Armour Perforation Test of Anti-Armour Ammunition,* Brussels: NATO, 1998.

[71] United States Department of the Army, *DETAIL SPECIFICATION: ARMOUR PLATE, STEEL, WROUGHT, HOMOGENEOUS (FOR USE IN COMBAT VEHICLES AND FOR AMMUNITION TESTING),* 2009.

[72] W. Arnold and F. K. Schäfer, “Behind Armor Blast (BAB) caused by shaped charges,” *International Journal of Impact Engineering,* vol. 23, no. 99, pp. 13-25, 1999.

[73] M. Nishida, H. Kato, K. Hayashi and M. Higashide, “Ejecta size distribution resulting from hypervelocity impact of spherical projectiles on CFRP laminates,” *Procedia Engineering,* vol. 58, pp. 533-542, 2013.

[74] A. A. Cenna, N. W. Page, E. Kisi and M. G. Jones, “Single particle impact tests using gas gun and analysis of high strain-rate impact events in ductile materials,” *Wear,* vol. 271, no. 9-10, pp. 1497-1503, 2011.

[75] A. Kolopp, S. Rivallant and C. Bouvet, “Experimental study of sandwich structures as armour against medium-velocity impacts,” *International Journal of Impact Engineering,* vol. 61, pp. 24-35, 2013.

[76] S. C. Zhao, Z. F. Song and X. P. Zhoa, “A potential approach to launch hypervelocity projectiles up to 10km/s based on two-stage gas gun facilities,” *Procedia Engineering,* vol. 58, pp. 98-109, 2013.

[77] L. Barker and R. Hollenbach, “Laser Interferometer for Measuring High Velocities of Any Reflecting Surface,” *Journal of Applied Physics,* vol. 43, pp. 4669-4775, 1972.

[78] D. H. Dolan, “Foundations of VISAR analysis,” Sandia National Laboratories, Albuquerque, NM and Livermore, CA, 2006.

[79] L. M. Barker, “VISAR vs PDV,” Valyn International, 12 June 2011. [Online]. Available: http://www.valynvisar.com/VISAR_vs_PDVLynn_M.pdf. [Accessed 2015 May 19].

[80] O. T. Strand and T. L. Whitworth, “Using the heterodyne method to measure velocities on shock physics experiments,” in *15th APS Topical Conference on Shock Compression of Condensed Matter*, Waikoloa, HI, 2007.

[81] G. Johnson and W. Cook, “A constitutive model and data for metals subjected to large strains, high strain rates and high temperatures,” in *7th International Symposium on Ballistics*, 1983.

[82] G. R. Johnson, “Numerical algorithms and material models for high-velocity impact computations,” *International Journal of Impact Engineering,* vol. 38, no. 6, pp. 456-472, 2011.

[83] D.-N. Zhang, Q.-Q. Shangguan, C.-J. Xie and F. Liu, “A modified Johnson–Cook model of dynamic tensile behaviors for 7075-T6 aluminum alloy,” *Journal of Alloys and Compounds,* vol. 619, pp. 186-194, 2015.

[84] J. Q. Tan, M. Zhan, S. Liu, T. Huang, J. Guo and H. Yang, “A modified Johnson–Cook model for tensile flow behaviors of 7050-T7451 aluminum alloy at high strain rates,” *Materials Science & Engineering A,* vol. 631, pp. 214-219, 2015.

[85] W. Song, J. Ning, X. Mao and H. Tang, “A modified Johnson-Cook model for titanium matrix composites reinforced with titanium carbide particles at elevated temperatures,” *Materials Science and Engineering A,* vol. 576, pp. 280-289, 2013.

[86] X. Wang, C. Huang, B. Zou, H. Liu, H. Zhu and J. Wang, “Dynamic behavior and a modified Johnson-Cook constitutive model of Inconel 718 at high strain rate and elevated temperature,” *Materials Science and Engineering A,* vol. 580, pp. 385-390, 2013.

[87] Q. Y. Hou and J. T. Wang, “A modified Johnson-Cook constitutive model for Mg-Gd-Y alloy extended to a wide range of temperatures,” *Computational Materials Science,* vol. 50, no. 1, pp. 147-152, 2010.

[88] W. K. Rule and S. Jones, “A Revised Form for the Johnson–Cook Strength Model,” *International Journal of Impact Engineering,* vol. 21, no. 8, pp. 609-624, 1998.

[89] R. W. Armstrong and F. J. Zerilli, “Dislocation Mechanics Based Analysis of Material Dynamics Behavior,” *Le Journal de Physique Colloques,* vol. 49, pp. 529-534, 1988.

[90] S. Tanimura, T. Tsuda, A. Abe, H. Hayashi and N. Jones, “Comparison of rate-dependent constitutive models with experimental data,” *International Journal of Impact Engineering,* vol. 69, pp. 104-113, 2014.

[91] H. W. Meyer, “A Modified Zerilli-Armstrong Constitutive Model Describing the Strength and Localizing Behavior of Ti-6Al-4V,” Army Research Laboratory, Aberdeen, MD, 2006.

[92] Z. Xu and F. Huang, “Comparison of constitutive models for FCC metals over wide temperature and strain rate ranges with application to pure copper,” *International Journal of Impact Engineering,* vol. 79, pp. 65-74, 2015.

[93] A. S. Khan, Y. S. Suh and R. Kazmi, “Quasi-static and dynamic loading responses and constitutive modeling of titanium alloys,” *International Journal of Plasticity,* vol. 20, pp. 2233-2248, 2003.

[94] J. R. Klepaczko, A. Rusinek, J. A. Rodríguez-Martínez, R. B. Pecherski and A. Arias, “Modelling of thermo-viscoplastic behaviour of DH-36 and Weldox 460-E structural steels at wide ranges of strain rates and temperatures, comparison of constitutive relations for impact problems,” *Mechanics of Materials,* vol. 41, pp. 599-621, 2009.

[95] S. Nemat-Nasser and J. Isaacs, “Direct measurement of isothermal flow stress of metals at elevated temperatures and high strain rates with application to Ta and Ta-W alloys,” *Acta Materialia,* vol. 45, pp. 907-919, 1997.

[96] S. Nemat-Nasser and W. Guo, “Flow stress of commercially pure niobium over a broad range of temperatures and strain rates,” *Materials Science and Engineering A,* vol. 284, pp. 202-210, 2000.

[97] S. Nemat-Nasser and W. Guo, “Thermomechanical response of DH-36 structural steel over a wide range of strain rates and temperatures,” *Mechanics of Materials,* vol. 35, pp. 1023-1047, 2003.

[98] A. Seeger, “The mechanism of glide and work hardening in face-centered cubic and hexagonal close-packed metals,” in *Dislocations and Mechanical Properties of Crystals*, New York, 1957.

[99] G. Z. Voyiadjis and F. H. Abed, “Microstructural based models for bcc and fcc metals with temperature and strain rate dependency,” *Mechanics of Materials,* vol. 37, pp. 355-378, 2005.

[100] S. Nemat-Nasser and Y. Li, “Flow stress of F.C.C. polycrystals with application to OFHC Cu,” *Acta Materialia,* vol. 46, no. 2, pp. 565-577, 1998.

[101] A. Rusinek and J. R. Klepaczko, “Shear testing of a sheet steel at wide range of strain rates and a constitutive relation with strain-rate and temperature dependence of the flow stress,” *International Journal of Plasticity,* vol. 17, pp. 87-115, 2001.

[102] A. Rusinek, J. A. Rodríguez-Martínez and A. Arias, “A thermo-viscoplastic constitutive model for FCC metals with application to OFHC copper,” *International Journal of Mechanical Sciences,* vol. 52, pp. 120-135, 2010.

[103] G. Chen, C. Ren, X. Qin and J. Li, “Temperature dependent work hardening in Ti–6Al–4V alloy over large temperature and strain rate ranges: Experiments and constitutive modeling,” *Materials & Design,* vol. 83, pp. 598-610, 2015.

[104] J. Donea, A. Huerta, J. Ponthot and A. Rodríguez-Ferran, “Arbitrary Lagrangian – Eulerian Methods,” in *Encyclopedia of Computational Mechanics*, Wiley, 1999.

[105] J. F. Moxnes, A. K. Prytz, Ø. Frøyland, S. Skriudalen, S. Børve and G. Ødegårdstuen, “Strain rate dependency and fragmentation pattern of expanding warheads,” *Defence Technology,* vol. 11, pp. 1-9, 2015.

[106] A. G. Petschek and L. D. Libersky, “Cylindrical Smoothed Particle Hydrodynamics,” *Journal of Computational Physics,* vol. 109, pp. 76-83, 1993.

[107] L. D. Libersky, A. G. Petschek, T. C. Carney, J. R. Hipp and F. A. Allahdadi, “High Strain Lagrangian Hydrodynamics,” *Journal of Computational Physics,* vol. 109, pp. 67-75, 1993.

[108] R. Stellingwerf and C. Wingate, “Impact modeling with smooth particle hydrodynamics,” *International Journal of Impact Engineering,* vol. 14, pp. 707-718, 1993.

[109] G. R. Johnson, R. A. Stryk and S. R. Beissel, “SPH for high velocity impact computations,” *Computer Methods in Applied Mechanics and Engineering,* vol. 139, no. 96, pp. 347-373, 1996.

[110] R. C. Batra and G. M. Zhang, “Modified Smoothed Particle Hydrodynamics (MSPH) basis functions for meshless methods, and their application to axisymmetric Taylor impact test,” *Journal of Computational Physics,* vol. 227, pp. 1962-1981, 2008.

[111] Air Force Armament Laboratory / Honeywell Inc., *User Instructions for the EPIC-2 Code,* Edina, MN, USA: Air Force Armament Laboratory, Air Force Systems Command, 1986.

[112] Ansys Inc., “Ansys Autodyn: Explicit Software for Nonlinear Dynamics,” 2007. [Online]. Available: http://www.esss.com.br/pdf/autodyn-11.pdf. [Accessed 03 June 2015].

[113] Dassault Systemes, “Abaqus/Explicit 6.14 Data Sheet,” 2014. [Online]. Available: http://www.3ds.com/fileadmin/PRODUCTS/SIMULIA/PDF/datasheets/simulia-abaqus-explicit-datasheet.pdf. [Accessed 03 June 2015].

[114] Livermore Software Technology Corporation, “LS-DYNA Theory Manual,” Livermore Software Technology Corporation, Livermore, CA, 2015.

[115] V. Hohler, K. Weber, R. Tham, B. James, A. Barker and I. Pickup, “Comparative analysis of oblique impact on ceramic composite systems,” *International Journal of Impact Engineering,* vol. 26, pp. 333-344, 2001.

[116] D. Bürger, A. Rocha De Faria, S. F. De Almeida, F. C. De Melo and M. V. Donadon, “Ballistic impact simulation of an armour-piercing projectile on hybrid ceramic/fiber reinforced composite armours,” *International Journal of Impact Engineering,* vol. 43, pp. 63-77, 2012.

[117] J. D. Hogan, J. G. Spray, R. J. Rogers, G. Vincent and M. Schneider, “Dynamic fragmentation of natural ceramic tiles: Ejecta measurements and kinetic consequences,” *International Journal of Impact Engineering,* vol. 58, pp. 1-16, 2013.

[118] M. J. Worsham, S. K. Treadway and A. D. Shirley, “Defeat of high velocity projectiles by a novel spaced armor system,” *Procedia Engineering,* vol. 58, pp. 338-347, 2013.

[119] M. Held, M. Mayseless and E. Rototaev, “Explosive reactive armor,” in *Proceedings of the 17th International Symposium on Ballistics,* Midrand, RSA, 1998.

[120] W. S. d. Rosset, “Patterned Armor Performance Evaluation for Multiple Impacts,” Army Research Laboratory, 2003.

[121] H. Dorsch, A. Bongartz and D. Rossberg, “Modelling of ballistic effects with regard to urban operations,” *27th International Symposium on Ballistics,* vol. 2013, pp. 591-601, 2013.

[122] H. Dorsch, A. Doerr, R. Hoellinger and A. Bongartz, “Modelling of behind wall debris effects,” *28th International Symposium on Ballistics,* pp. 1462-1470, 2014.

[123] W. Arnold and W. Paul, “Behind armor debris investigation and their application into a new vulnerability model,” *International Journal of Impact Engineering,* vol. 26, pp. 21-32, 2001.

[124] E. Wielewski, G. J. Appleby-Thomas, P. J. Hazell and A. Hameed, “An experimental investigation into the micro-mechanics of spall initiation and propagation in Ti-6Al-4V during shock loading,” *Materials Science and Engineering A,* vol. 578, pp. 331-339, 2013.

[125] P. J. Hazell, G. J. Appleby-Thomas, E. Wielewski, C. Stennett and C. Siviour, “The influence of microstructure on the shock and spall behaviour of the magnesium alloy, Elektron 675,” *Acta Materialia,* vol. 60, no. 17, pp. 6042-6050, 2012.

[126] R. A. Barrett, P. E. O'Donoghue and S. B. Leen, “A dislocation-based model for high temperature cyclic viscoplasticity of 9-12Cr steels,” *Computational Materials Science,* vol. 92, pp. 286-297, 2014.

[127] B. Golden, D. Li, N. O'Dowd and P. Tiernan, “Microstructural Modelling of P91 Martensitic Steel Under Uniaxial Loading Conditions,” *Journal of Pressure Vessel Technology,* vol. 136, no. April, pp. 1-6, 2013.

[128] D.-F. Li, B. J. Golden and N. P. O’Dowd, “Multiscale modelling of mechanical response in a martensitic steel: A micromechanical and length-scale-dependent framework for precipitate hardening,” *Acta Materialia,* vol. 80, pp. 445-456, 2014.

[129] N. Jacques, S. Mercier and A. Molinari, “A constitutive model for porous solids taking into account microscale inertia and progressive void nucleation,” *Mechanics of Materials,* vol. 80, pp. 311-323, 2015.

[130] C. Sartori, S. Mercier, N. Jacques and A. Molinari, “Constitutive behavior of porous ductile materials accounting for micro-inertia and void shape,” *Mechanics of Materials,* vol. 80, pp. 324-339, 2015.

[131] A. Molinari and S. Mercier, “Micromechanical modelling of porous materials under dynamic loading,” *Journal of the Mechanics and Physics of Solids,* vol. 49, pp. 1497-1516, 2001.

[132] A. Molinari, S. Mercier and N. Jacques, “Dynamic failure of ductile materials,” *Procedia IUTAM,* vol. 10, pp. 201-220, 2013.

[133] C. Czarnota, N. Jacques, S. Mercier and A. Molinari, “Modelling of dynamic ductile fracture and application to the simulation of plate impact tests on tantalum,” *Journal of the Mechanics and Physics of Solids,* vol. 56, pp. 1624-1650, 2008.

[134] C. E. Anderson and J. (. P. Riegel, “A penetration model for metallic targets based on experimental data,” *International Journal of Impact Engineering,* vol. 80, pp. 24-35, 2015.

[135] F. Dunne and N. Petrinic, Introduction to Computational Plasticity, 2 ed., Oxford, UK: Oxford University Press, 2005.

[136] The Aluminum Association, Inc., “International Alloy Designations and Chemical Composition Limits for Wrought Aluminum and Wrought Aluminum Alloys,” The Aluminum Association, Inc., Arlington, VA, USA, 2015.

[137] R. Bauri, D. Yadav, C. Shyam Kumar and B. Balaji, “Tungsten particle reinforced Al 5083 composite with high strength and ductility,” *Materials Science and Engineering: A,* vol. 620, pp. 67-75, 2015.

[138] G. Heilig, N. Durr, M. Sauer and A. Klomfass, “Mesoscale Analysis of Sintered Metals Fragmentation under Explosive and Subsequent Impact Loading,” *The 12th Hypervelocity Impact Symposium,* vol. 58, pp. 653-662, 2013.

[139] B. Srivathsa and N. Ramakrishnan, “Ballistic performance maps for thick metallic armour,” *Journal of Materials Processing Technology,* vol. 96, pp. 81-91, 1999.

[140] Z. Rosenberg and E. Dekel, “Revisiting the perforation of ductile plates by sharp-nosed rigid projectiles,” *International Journal of Solids and Structures,* vol. 47, no. 22-23, pp. 3022-3033, 2010.

[141] V. Ikkurthi and S. Chaturvedi, “Use of different damage models for simulating impact-driven spallation in metal plates,” *International Journal of Impact Engineering,* vol. 2004, no. 30, pp. 275-301, 2004.

[142] E. Strassburger, M. Hunzinger, P. Patel and J. W. McCauley, “Analysis of the Fragmentation of AlON and Spinel Under Ballistic Impact,” *Journal of Applied Mechanics,* vol. 80, no. May, p. 031807, 2013.

Figures and Tables

Table 1: Prominent metals used for vehicle armour, along with selected properties.

Material	**Density** *(kg/m³)*	**Yield Strength** *(MPa)*	**Specific Strength** *(MN.m.kg^{-1})*	**References**
Al 5083	2660	156	0.0586	[136], [137]
Al 7039	2740	337	0.1230	[136], [138]
RHA	7850	933	0.1189	[36]
HHA	7850	1250 to 1500	0.1592 to 0.1911	[18]
Ti-6Al-4V	4550	990	0.2176	[139]
Mild Steel	7800	325	0.0417	[139]

Table 2: Summary of strength models analysed in this review.

Model	**Year**	**Description**	**References**
Johnson-Cook (JC)	1983	Flow stress is a function of strain, strain rate and temperature, three empirical constants and two empirical exponents.	[81] [82]
Revised Johnson-Cook	1998	Two additional empirical constants are added, taking account of sudden strengthening which takes place in some metals at high strain rates (>10^4 s^{-1})	[88]
Zerilli-Armstrong (ZA)	1987	Makes a distinction between materials with BCC lattice structures (e.g. α-iron) and FCC structures (e.g. copper). Flow stress is a function of strain, strain rate, temperature and six material constants.	[89] [90]
Tanimura-Mimura	2009	Materials organised into characteristic groups. A number of material constants based on this group and the material's quasi-static stress-strain curve are required.	[90]
Khan-Huang-Liang	2003	Developed using experimental data of Titanium alloys. Increased strain rates lead to decreased work hardening.	[93]
Physical Base (PB)	1957/ 1975	Breaks the total stress into two contributions: an athermal component which is independent of temperature and strain rate, and a thermally activated second component which takes these factors into account.	[94] [95] [96] [97] [98]
Nemat-Nasser-Li	1998	Similar to the PB model, i.e. based on addition of athermal and thermally activated components of stress. Requires at least six material constants.	[100]

Rusinek-Klepaczo	2001	Similar to the PB model, i.e. based on addition of athermal and thermally activated components of stress. Requires up to ten material constants.	[101] [102] [94]
Voyiadjis-Abed	2005	Has different expressions for flow stress depending on FCC or BCC, as with the ZA model, but claims to be more accurate since it uses an exact value rather than an approximation which was claimed to be valid in the ZA model.	[99]

Table 3: Published material properties for the JC, ZA and KHL models for Ti-6Al-4V.

Model	**Material Properties**								**Source**
	A (MPa)	B (MPa)	n -	C -	m -				
JC	1104	1036	0.6349	0.0139	0.7794				[93]
	C_0 (MPa)	C_1 (MPa)	C_2 (MPa)	ε_r	$\dot{\varepsilon}_\beta$ (s^{-1})	$\dot{\varepsilon}_\alpha$ (s^{-1})	β_0 (K^{-1})	α_0 (K^{-1})	
ZA	1217	139	3955	0.1877	1.6×10^4	8.25×10^5	1.59×10^{-2}	7.55×10^{-3}	[91]
	A (MPa)	B (MPa)	n_1	n_0	C	m	D_0 (s^{-1})		
KHL	1069	874.8	0.5456	0.4987	0.02204	1.3916	10^6		[93]

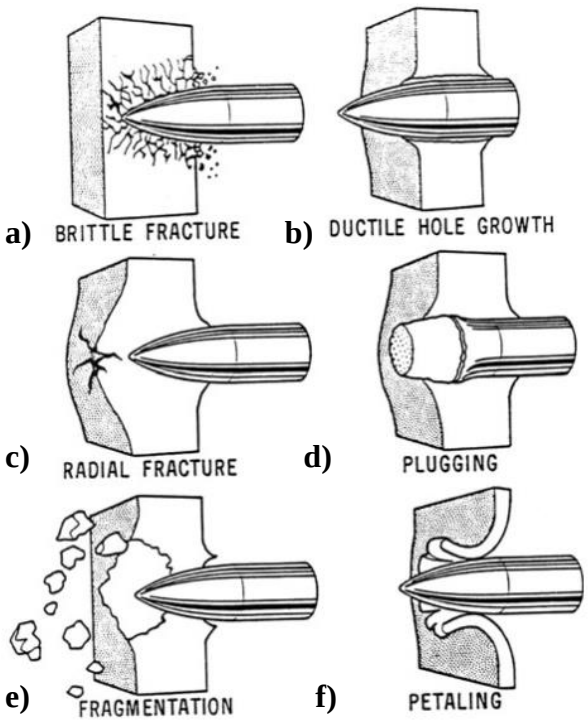

Fig. 1: Different failure modes for armour [4].

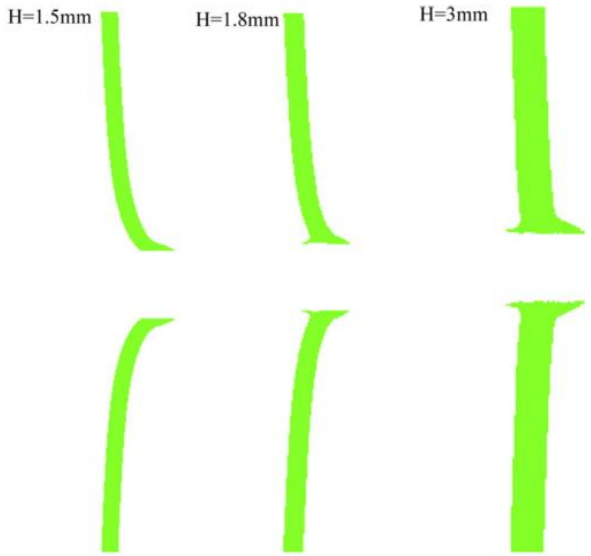

Fig. 2: Comparison of penetration failure in plates of varying thickness, from Finite Element Analysis (FEA). The greater deformation of thinner plates prior to failure (dishing) can be clearly seen (H=1.5mm), as can the characteristic bulge of deformed material from ductile hole enlargement (thickest plate) (H=3mm). Figure reprinted from [140], with permission from Elsevier.

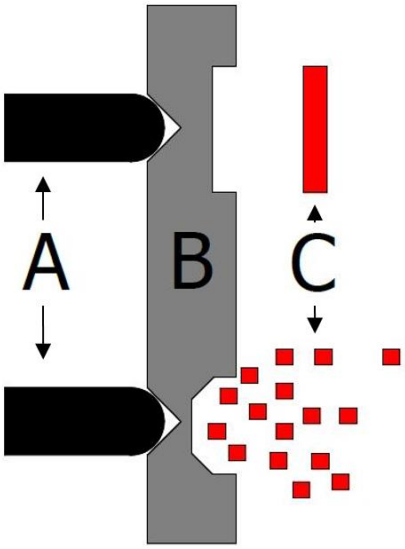

Fig. 3: General diagram of the spalling process showing the impacting projectiles A (the ‘flyers’), the target material B, and the resulting spall fragment or fragments C.

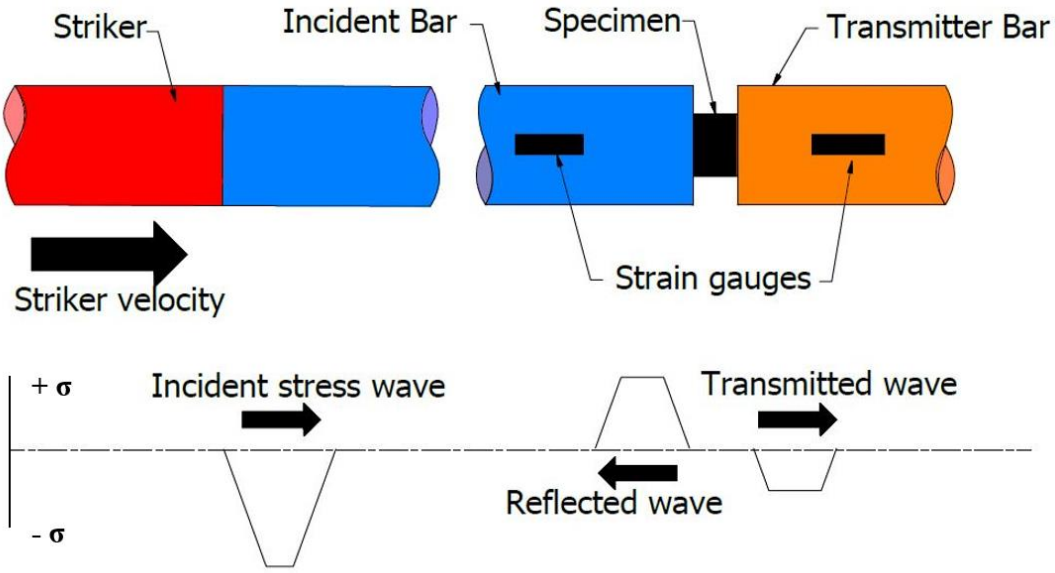

Fig. 4: Schematic diagram of Split Hopkinson pressure bar apparatus.

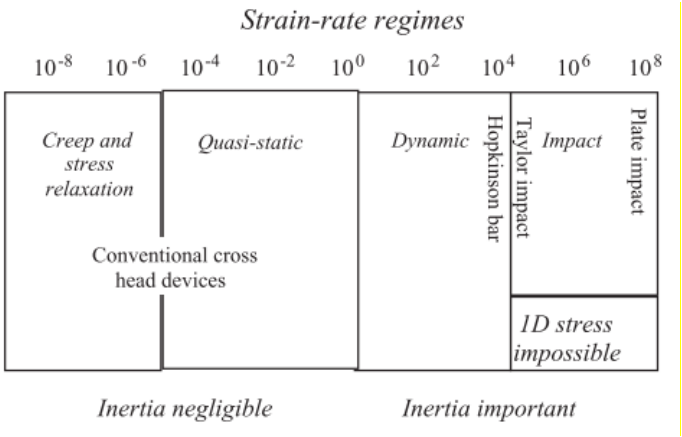

Fig. 5: A wide range of strain rates, measured in units of s^{-1}, and the various experimental techniques which are valid. Reprinted from [62] with permission from Elsevier.

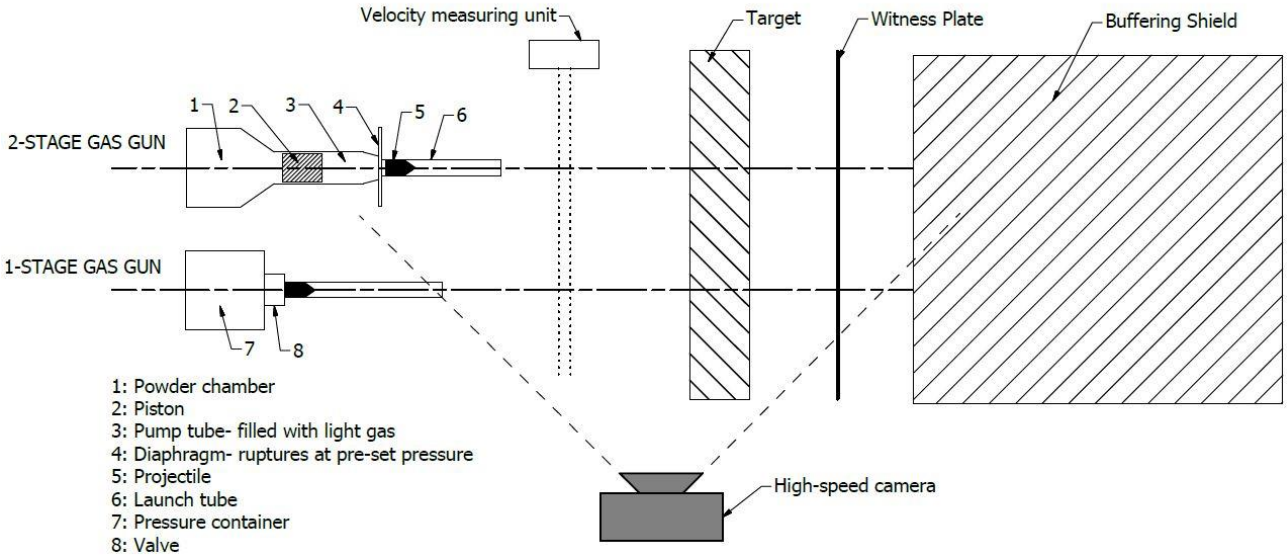

Fig. 6: Simple schematic of a gas-gun test facility, including instrumentation for gathering data. Two different kinds of gas-guns are shown.

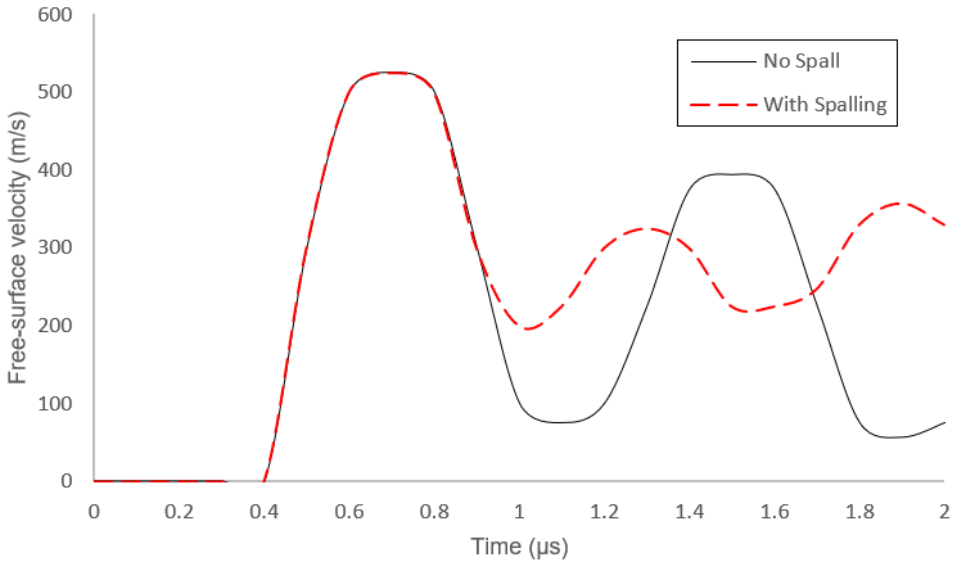

Fig. 7: Generic plot of free-surface velocity as a function of time following an impact, adapted from [141]. Note where the two curves clearly separate—this is the time at which spall occurs.

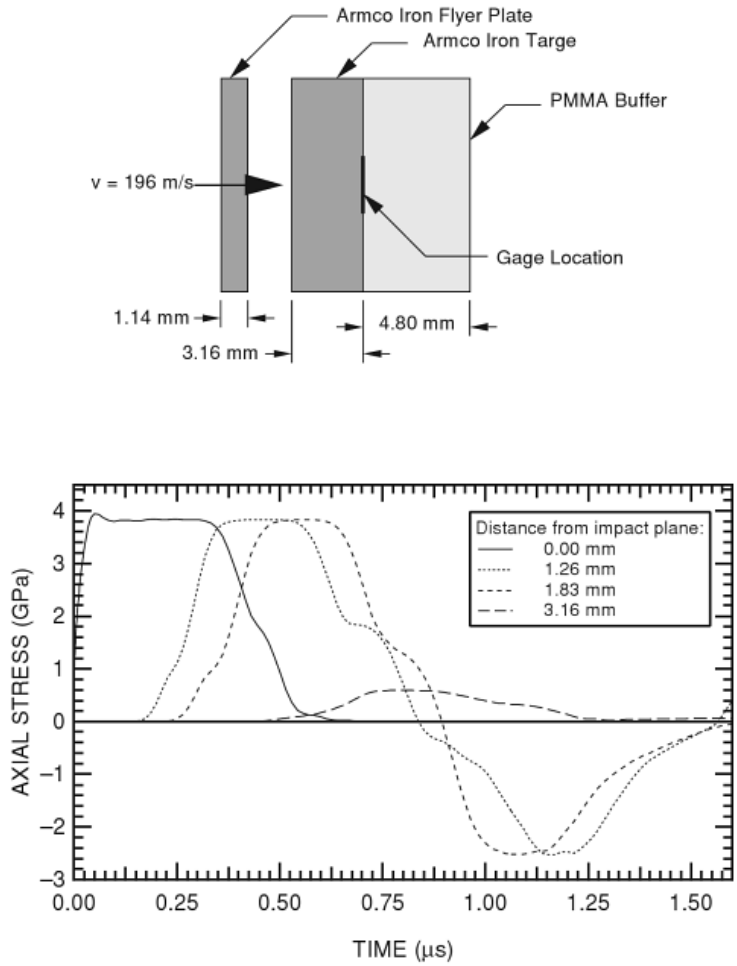

Fig. 8: Typical experimental setup and plotted results from a spallation experiment [53]. Not shown, but usually included in the setup, is a means of measuring the flyer velocity. This usually consists of a pair of light beams which the projectile breaks, or a set of high-speed cameras [142]. Figure reprinted from [53] with permission from Springer.

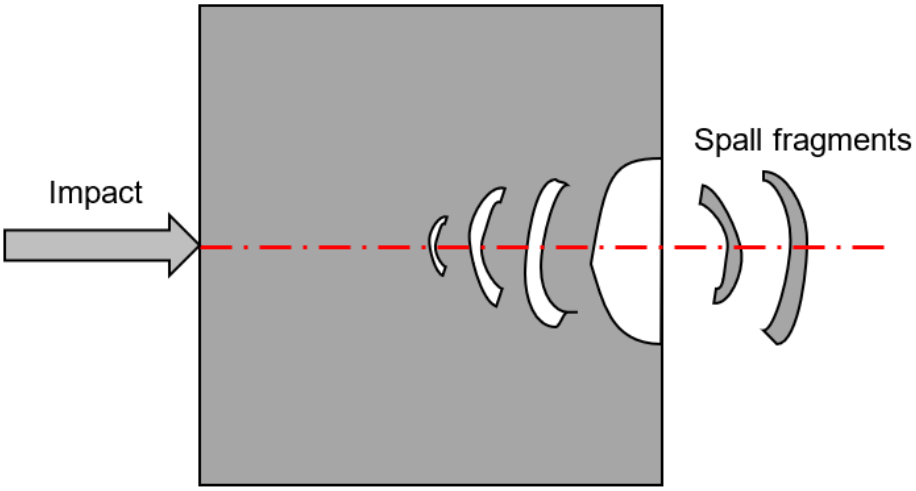

Fig. 9: Schematic diagram, adapted from [57], showing how a greater amount of fragmentation occurs near the axis of the projectile, while a smaller amount of fragmentation away from this axis has the effect of maintaining the integrity of the material.

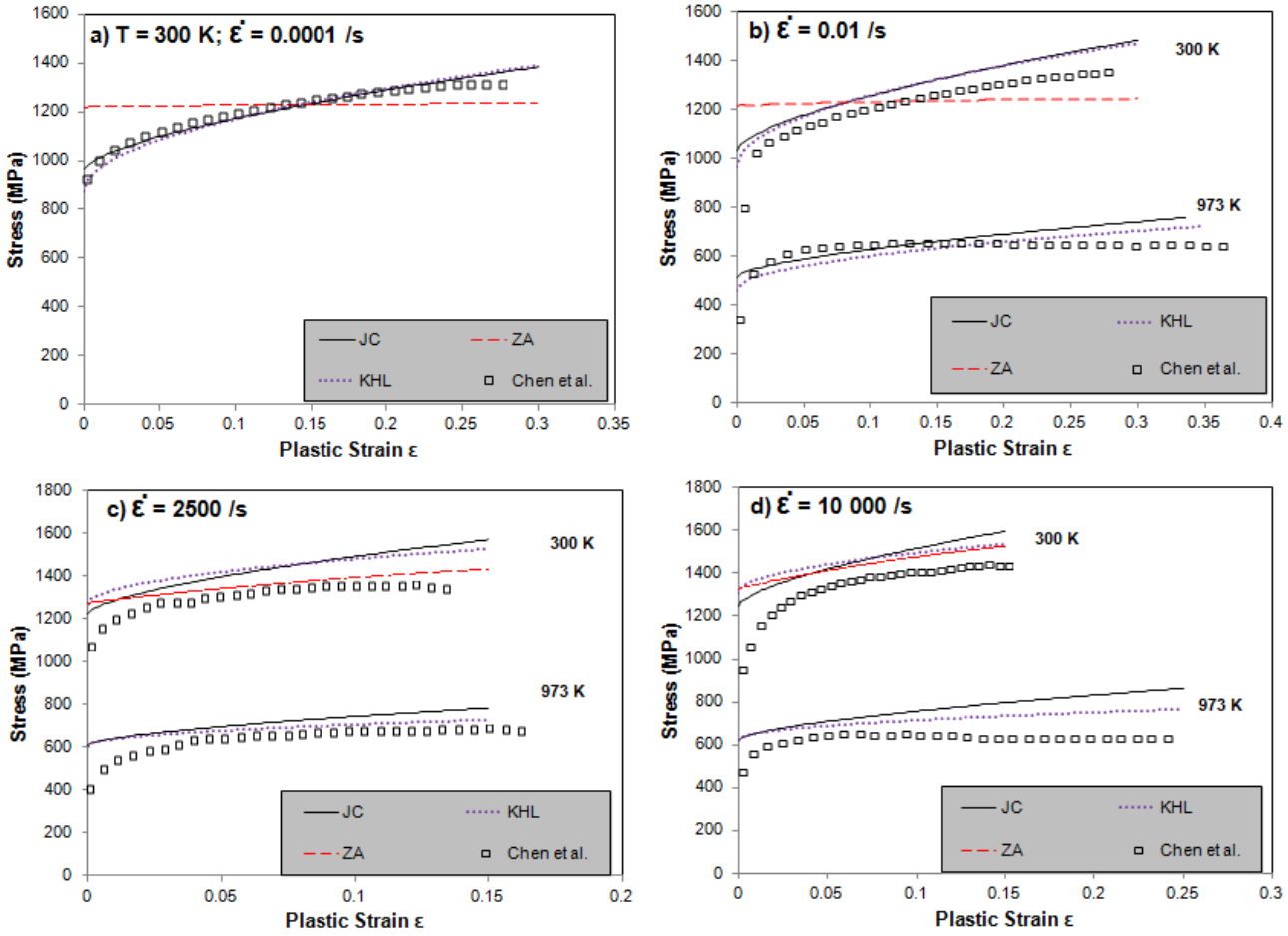

Fig. 10: Comparison of the Johnson-Cook (JC), Khan-Huang-Liang (KHL) and Zerilli-Armstrong (ZA) constitutive models for Ti-6Al-4V via uniaxial stress-strain curves. The models are compared with experimental results presented by Chen et al. [103]. There is no particular significance to the temperatures chosen, apart from highlighting the effect of temperature-softening on the material.

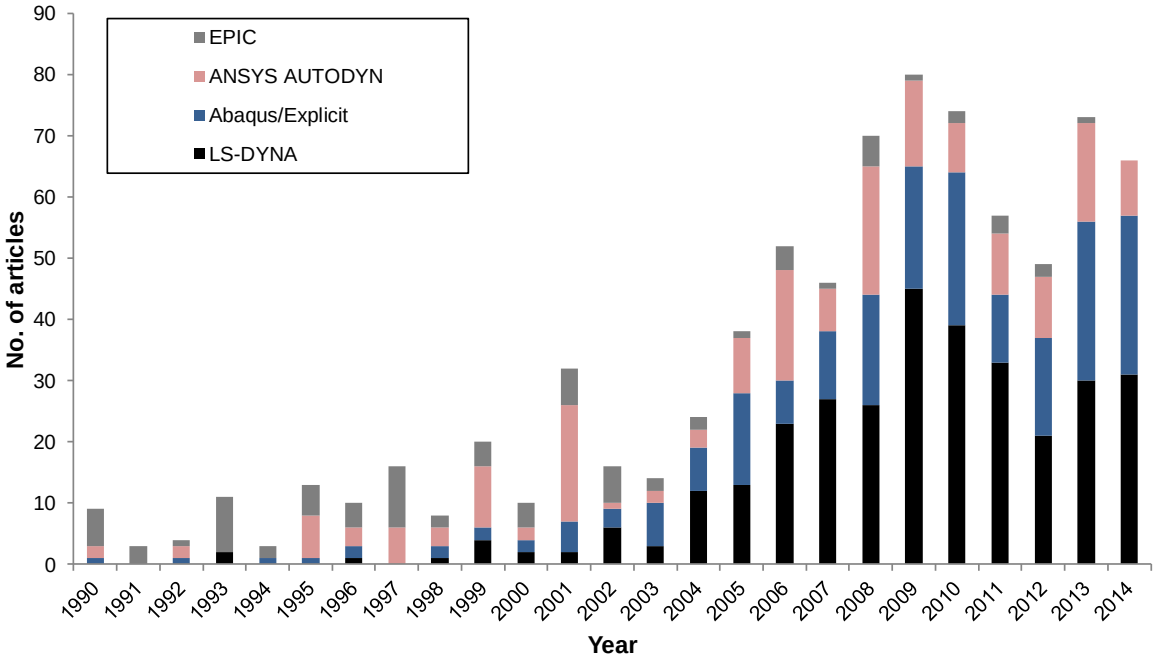

Fig. 11: Chart showing the popularity of four leading FEA codes used for impact simulations over time. The primary axis pertains to the bar chart, and is simply the number of articles for each type of code, stacked cumulatively.

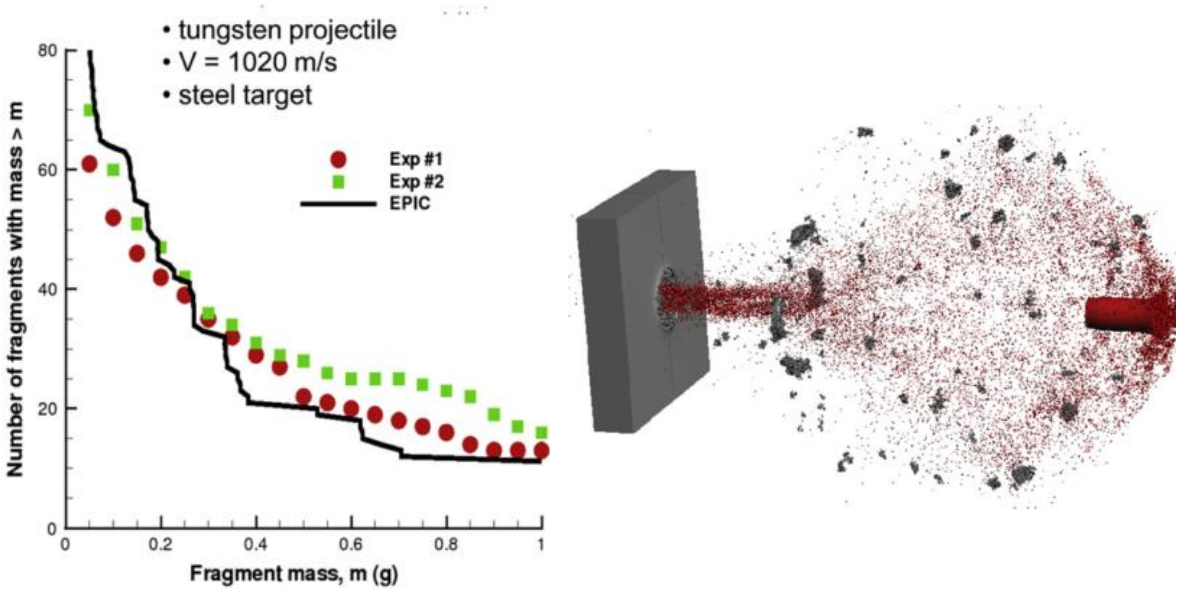

Fig. 12: Comparison of experimental and numerical simulation of a tungsten projectile impacting a steel target with a velocity of 1020 m/s. The graph on the left shows the close correlation between simulation (EPIC code) and experiments. The image on the right, from the numerical simulation, shows the complete penetration of the target and the large cloud of spall material. Reprinted from [82] with permission from Elsevier.

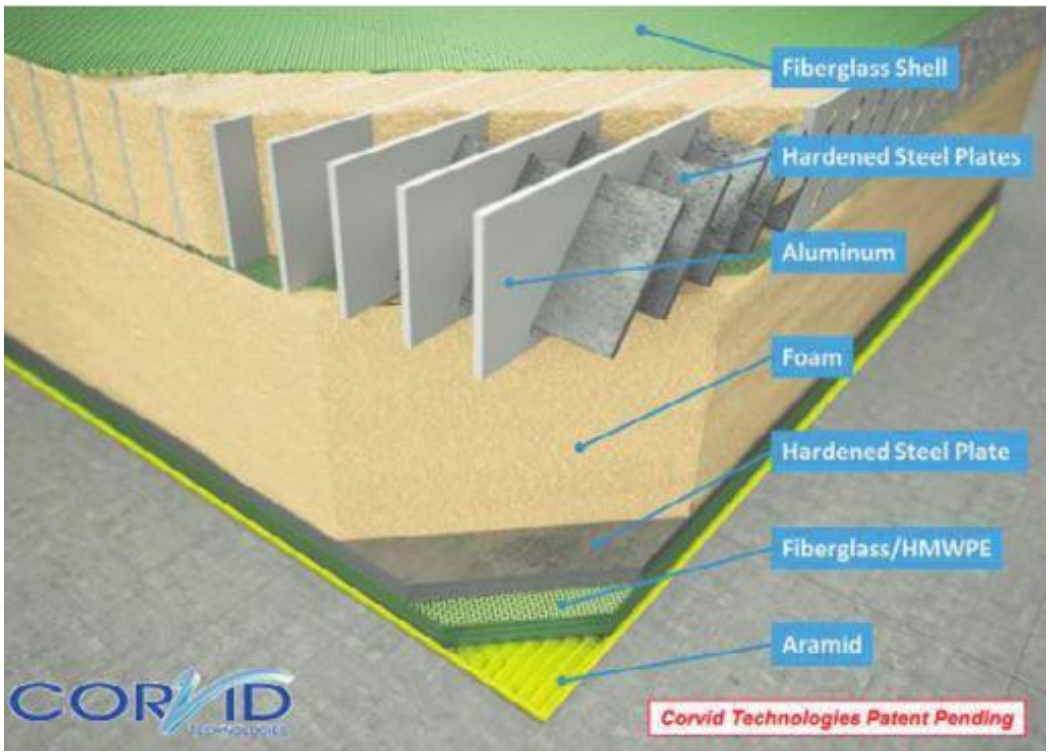

Fig. 13: A proposed spaced armour system, in which different materials and geometries are spaced at different layers in order to have different effects on a penetrator as it passes through. Reprinted from [118] with permission from Elsevier.

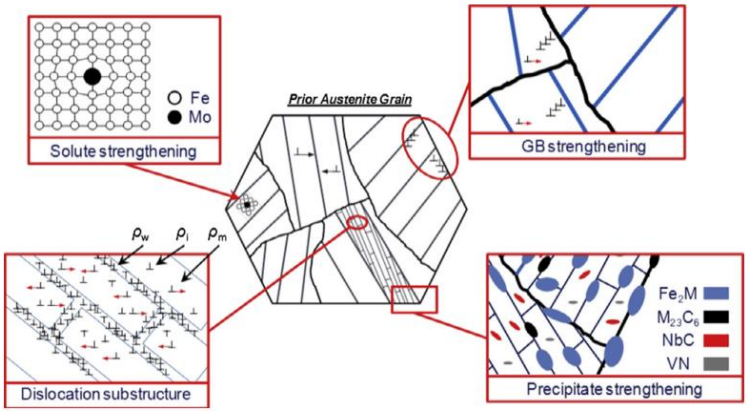

Fig. 14: Schematic representation of the hierarchical grain structure of 9-12Cr steel (P91), showing various strengthening mechanisms. Reprinted from [126] with permission from Elsevier.

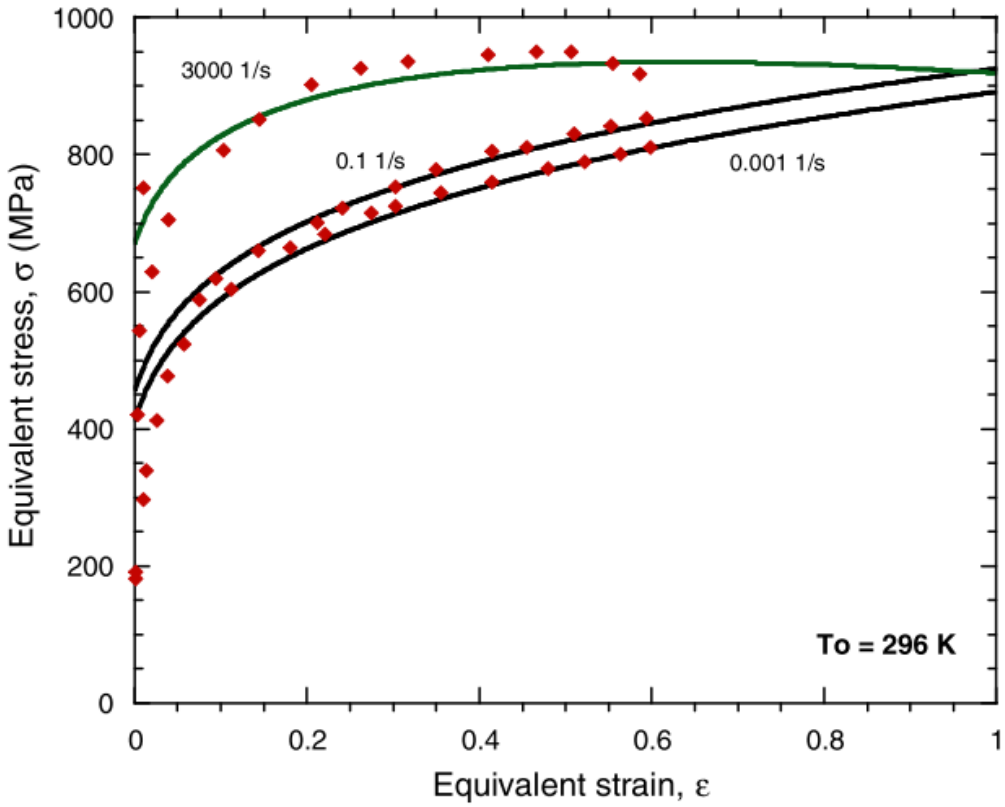

Fig. 15: An illustration of the performance of a physically-based model. The RK constitutive model, presented by Rusinek and Klepaczko [94] and described in Section 5.1.7, is compared to experimental stress-strain data at a variety of strain rates. The material used is DH-36 steel. Reprinted from [94] with permission from Elsevier.